*Egypt. J. of Appl. Sci., 40 (5-6) 2025* *61-100*

# PETROGENESIS AND MINERALIZATION OF THE ABU DABBAB ALBITE GRANITE: INSIGHTS INTO RARE-METAL A-TYPE GRANITES IN THE ARABIAN–NUBIAN SHIELD

**Moustafa M. Mogahed[1*]; Maher A. El Amawy[1] ; Asran M. Asran[2] ; Nesma G. Mahmoud[1]**

1Geology Department, Faculty of Science, Benha University, 13518, Benha, Egypt
2Geology Department, Faculty of Science, Sohag University, 82524, Sohag, Egypt
***E-mail mustafa.ahmed01@fsc.bu.edu.eg**

## ABSTRACT

The Arabian–Nubian Shield (ANS), spanning northeast Africa and the Arabian Peninsula, evolved during the Neoproterozoic collision of East and West Gondwana and the closure of the Mozambique Ocean. Following a significant post-collisional phase beginning around 620 Ma, the ANS stabilized by 540 Ma and witnessed intrusive events featuring rare-metal–enriched granitoids. Among these, the Abu Dabbab albite granites (ADG) in Egypt's Central Eastern Desert stand out due to their high concentrations of Nb, Ta, Sn, Zr, and REEs, and their petrogenesis remains debated. Our integrated field, petrographic, mineralogical and geochemical investigations reveals that the ADG are peraluminous, high-SiO□, highly fractionated calc-alkaline plutons emplaced ANS's transitional tectonic regime. ADG characterized by high Rb/Sr, elevated Nb–Ta–Sn–Hf contents and strong negative Eu anomalies aligning with muscovite-bearing, evolved A-type granite suites with substantiate a crustal source influenced by juvenile mantle-derived underplating. We propose a petrogenetic model where lithospheric thinning and magmatic underplating triggered hydration and melting of micas-rich crustal rocks. The resultant F-rich, peraluminous melts underwent prolonged fractional crystallization under magmatic–hydrothermal conditions, producing Ta–Nb–Sn mineralization and greisen–vein systems.

**Key Words:** Arabian-Nubian Shield; Abu Dabbab granite; Alkali granite; Fractional crystallization, Lithospheric thinning; crustal source.

## INTRODUCTION

During the Neoproterozoic, the Arabian–Nubian Shield (ANS)—spanning much of Northeast Africa and the Arabian Peninsula—formed as East and West Gondwana converged, resulting in the closure of the Mozambique Ocean **(Stern, 1994).** Following the main collision phase, the ANS entered a post-orogenic period around 620 Ma, ultimately evolving into a stable cratonic and platform environment by approximately 540 Ma **(Johnson and Woldehaimanot, 2003)**. The ANS is marked by the presence of many post-collisional rare metal-bearing granites and pegmatites **(Renno *et al.*, 1993 ; Eliwa *et al.*, 2014 ; Abdelfadil *et al.*, 2016; Mogahed and**

**Abdelfadil, 2021 ; Abdelfadil *et al.*, 2022b and Sami *et al.*, 2022).** These late stage intrusions range from calc-alkaline to alkaline granitoids, and show varying degrees of metasomatism **(Abdelfadil *et al.*, 2022c)**. In particular, most of these intrusions are evolved high-K calc-alkaline and shoshonitic granitoids that are grouped as A-type granitoids **(Liegeois *et al.*, 1998)**. The widespread of this group within the ANS (Fig. 1a) have attracted significant interests due their economic value as a fundamental resources (e.g., Nb, Ta, U, Zr, Th and rare-earth elements) **(Abdelfadil *et al.*, 2022a)**. In spite of a multitude of studies due to their frequent occurrences, the genesis and geotectonic history of these granitoids, as well as their rare metal mineralization, remain contentious topics **(Azer *et al.*, 2019b and Mahdy *et al.*, 2020)**.

Rare-metal granites within the Nubian Shield are typically linked to Nb–Ta and Sn mineralization, yet their magmatic and hydrothermal development—and how these relate to such mineralization—remains insufficiently understood. The Abu Dabbab granites (ADG), found in the Egyptian CED, offer a valuable case study to refine our understanding of rare-metal granite formation and associated ore processes. These granites are dominated by albite, orthoclase, quartz, and lithium-rich phengite, with lesser amounts of cassiterite, columbite-tantalite, wodginite, and hafnium-rich zircon **(Sami *et al.*, 2022)**.

Abu Dabbab granite (ADG) are significantly enriched in rare metals (e.g., Nb, Ta, Zr, and REEs) **(Abuamarah *et al.*, 2021 and Azer *et al.*, 2023)**, but its origin and tectonic evolution is still case of controversy. Some researchers argue that the Abu Dabbab granite is a classic post-collisional A-type granite formed primarily by fractional crystallization of subcontinental lithospheric mantle (SCLM) and lower crustal melts triggered by lithospheric thinning and underplating **(Sami *et al.*, 2022)**, whereas some authors described it as plagiogranite that are related to mantle source and associated with ophiolitic sequence **(El-Desoky *et al.*, 2022)** and others demonstrated that ADG originated through primitive, mantle-derived basaltic melts interacted with the partially melted oceanic crustal material, generating hybrid magmas. These mixed melts then underwent fractional crystallization, evolving into tonalitic compositions before finally differentiating into an $A_1$-type granite. $A_1$ granites are typically mantle-sourced and associated with ocean-island or intraplate settings **(Heikal *et al.*, 2019)**. Accordingly, in order to resolve these competing descriptions, we present in this study the results of detailed field observations, petrochemical analysis and mineralisation data that are aimed to provide a clearer understanding of the Abu Dabbab granite magma source and its petrogenesis, and to interpret these data through the ANS's geodynamic framework.

**General Geology**

The area of Abu Dabbab located in the Central Eastern Desert of Egypt north Idfu-Marsa Alam asphaltic road, about 30 km north of Marsa Alam, and extends for 10 km west of the Red Sea coast. It covers an area of about 340 $Km^2$ and is limited by the Latitudes 25° 8′ 00″- 25° 25′ 00″N and Longitudes 34° 25′ 00″- 34° 45′00″ E (Fig. 1). It constitutes four principal lithological complexes (Fig. 1); dismembered ophiolites, island arc-volcanics, metagabbro-diorite complex and the granitoids (Figs. 1c).

Dismembered ophiolites are represented by ultramafic rocks and highly sheared ultramafic rocks with rare slices of ophiolitic metagabbro. The ultramafic rocks are mostly serpentinized and tectonically incorporated within a matrix of highly sheared ultramafic derivatives and dissected by chrysotile veinlets (Fig. 2a). There is no thermal effect along the contact between serpentinites and their surrounding rock regarding that these serpentinites are allochtonous and coinciding with the main strike of ultramafic rock of the Central Eastern Desert. The ophiolitic metagabbros are less common, occur essentially as rare slices within the highly sheared ultramafic rocks in the northern side of Wadi Abu Dabbab and farther the southwestern part of the study area. Mostly, the ophiolitic metagabbro are transformed into amphibolites (Fig. 2b).

Island arc metavolcanics are widespread in the present area and made up of mainly basic metavolcanics and highly sheared their derivatives (e.g, hornblende schist, epidote chlorite schist and chlorite schist), whereas the volcanoclastics metasediments are mainly represented by metatuffs (Fig. 2c).

Metagabbro-diorite complex covers most of the mapped area (Fig. 1) and are intruding the pre-existing rocks (e.g: dismembered ophiolites and island arc volcanic). They form high to moderate relief, displaying dark to gray colour and follow dilation fractures forming cross-cutting dykes. The rocks possess massive and less deformed core but are characterized by highly foliations and shearing towards their margins (Fig. 2d).

Along Wadi Abu Dabbab, the granitoid rocks are classified into three main groups: Granodiorite and relics of tonalite, monzogranite and Albite granite.

Granodiorites have intruded into the metavolcanics and exhibit gneissic texture due to the deformation (Fig. 2e)**.** Monzogranites were intruded into the pre-existing rocks and, sometimes, are tapering along the attitude of foliation planes of the highly sheared metagabbro-diorite rocks. These rocks are characterized by moderate to high topography with pink to pale red colour.

Abu Dabbab Albite granite (ADG) which is the main objective of this study regarded as the youngest granites in the study area. They are formed in the late stages of crystallization where the following elements were

concentrated; Sn, Nb, Ta and rare earths. ADG is fine- to medium- grained with pronounced white colour. It has a shape of sheet-like body (Fig. 2f) and occurs as slices cutting across the foliations of the country rocks and, sometimes, parallel to them (Fig. 2f). It displays intrusive contact against their country rocks that is mostly characterized by shearing, with occasionally flower structure (Fig. 2g). The body of ADG attains long axis striking N70-80W nearly about (0.4 km) and 470m high and is controlled by NNW-SSE and ~N-S, NE- and NW- striking fault/fracture zones (Fig. 2g). In the marginal zones of the ADG, hydrothermal fluids exert a pronounced influence, leading to intense secondary mineral replacement. This metasomatic overprint is evidenced by the extensive formation of shear zones, pegmatites, greisen, and quartz pods and veins along fracture networks (Fig. 2h). During the greisenization process, primary phases such as albite, perthite, and muscovite are progressively replaced. New generations of minerals, including quartz, muscovite, topaz, fluorite, cassiterite, and wolframite are deposited , where the original assemblage is consumed.

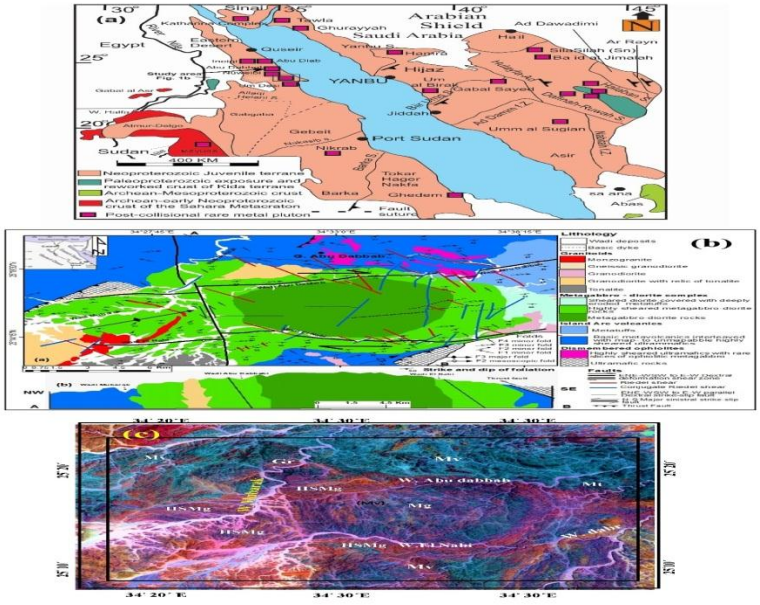


**Fig. 1.** (a) ANS Geological map illustrates the location of Abu Dabbab area and other major granitic post-collisional rare metal-bearing plutons. (b) Geologic map of the Wadi Abu Dabbab-Wadi El Nabi area, modified after EGSMA (1991) with A-B Vertical exaggerated cross section taken along NW-SE direction. (c) RGB false color landsat image of the Study area showing some of the present rock units; the metavolcanis (Mv), metatuffs (Mt), the metagabbro-diorite rocks (Mg), the highly sheared metagabbro-diorite rocks (HSMg) and granodiorite (Gr).

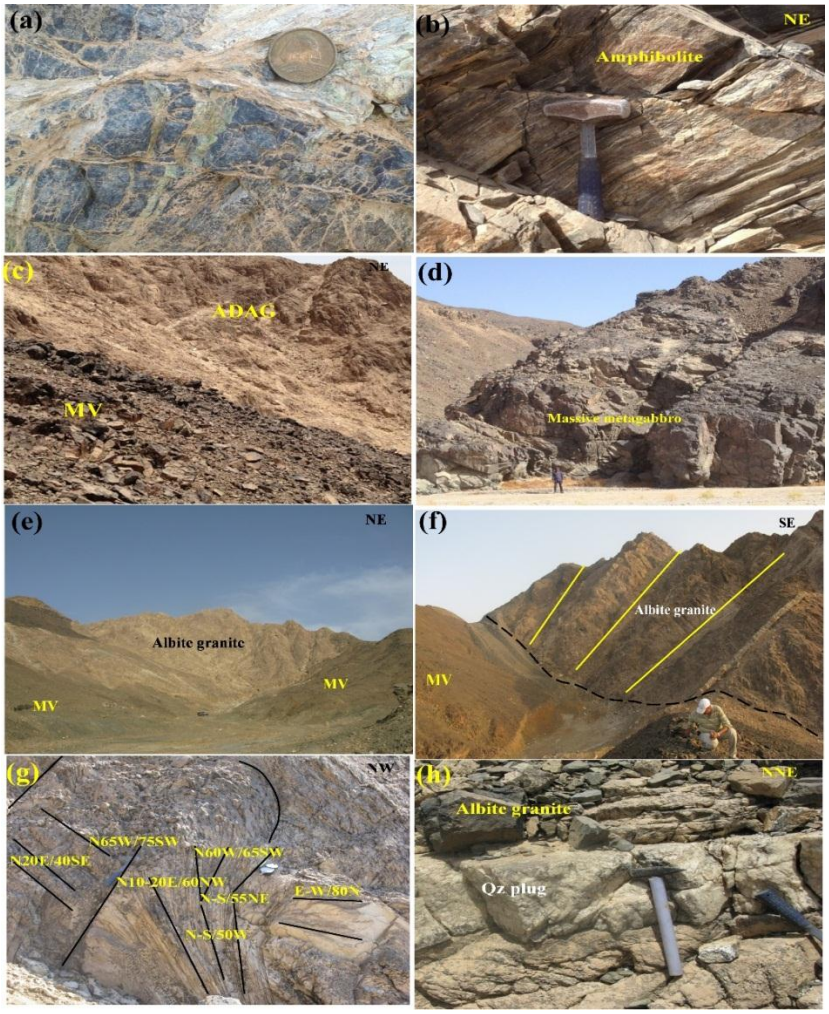


**Fig. 2:** Field photographs of the of Abu Dabbab area. (a) Chrysotile veinlets within the ultramafic rocks serpentinite. (b) Amphibolite rocks; striking N40-50E/40-50 SE in the south western part of the study area. (c) Intrusive contact between the highly sheared metavolcanic (MV) and Abu Dabbab albite granite (ADG). (d) Massive and less deformed metagabbro along the northern in the southeastern part of the study area (e) Abu Dabbab albite granite stands as a white hill caping the highly sheared ultramafic and metavolcanic rocks. (f) Dashed black line defines the intrusive contact of the albite granite cutting across the foliations of the metavolcanics (Mv). White lines represent locations of shear joints in the granite body. (g) Flower structure indicative of highly shearing in the mineralized albite granite in the southeastern part of the pluton. (h) Quartz plugs along the margin of albite granite in the northeastern side of the pluton.

**Petrography**

In this section we will discuss only the Abu Dabbab albite only which is the main objective of this study. ADG is mainly fine- to medium-grained. Microscopically, this rock is mainly composed of albite, quartz, microcline, orthoclase and mica (Fig. 3ad). Zircon, columbite, pyrochlore, apatite, allanite, zircon, tapiolite, cassiterite, fluorite, xenotime and rutile are the accessories (Figs. 3e and f).

Albite occurs as tabular crystals. Locally, albite crystals overgrow on K- feldspars of orthoclase and microcline (Figs. 3a and b). Quartz occurs as colorless shapeless crystals, displays wavy extinction and, sometimes, the quartz crystals overgrown on albite due to silica leaching (Fig. 3c). Quartz phenocrysts often contain clusters of fluid inclusions and albite grains, forming what is known as a "snowball texture." In this texture, larger albite crystals are concentrated at the core of the phenocrysts, while finer albite grains occupy the mantle (Fig. 3d). This feature results in a distinctive, zoned appearance where the centres appear denser, surrounded by a ring of smaller albite inclusions. Microcline forms subhedral prismatic crystals and exhibits cross-hatching twinning. Muscovite occurs as disseminated grains or clustered subhedral flakes, and is commonly associated with, zircon, apatite and rutile. Apatite is high relief, colourless and occurs as small euhedral to subhedral elongate prismatic crystals**.** Zircon occurs as small crystals with high relief.

The quartz porphyroclasts range in diameter between 2 and 3mm. Alkali feldspars occur as orthoclase, microcline, and microcline perthite. Perthite occurs as euhedral to subhedral crystals reaching up to 5 mm in length and exhibiting flame- and string-like perthitic intergrowths. The microcline shows cross-hatched twinning (Fig. 3c). Plagioclase minerals are sodic in composition ranging from albite to oligoclase ($An_{10-18}$) and occur as porphyroclasts and/or stretched crystals alongside quartz and K-feldspars forming fine groundmass (Figs. 3b and d). Most plagioclase porphyroclasts display albite twinning along with albite-Carlsbad twins. The plagioclase shows deformation and micro faulting of twin lamellae (Fig. 3e). Many zircon, apatite, as well as quartz inclusions are common within plagioclase crystals. Biotite appears as small brown flakes aligned in a consistent direction (Fig. 3f). Muscovite occurs as wide spread flakes that are generally fractured and corroded by quartz, perthite and plagioclase (Figs. 3b and F). Zircon forms anhedral to subhedral crystals (Fig. 3e) associated with muscovite. The biotite shows pleochroic haloes surrounding the zircons (Figs. 3f and g). Fluorite generally occurs interstitial grain, whereas secondary uranium minerals occur as radial crystals in zircon (Fig. 3e); they are rimmed by opaques and are associated with plagioclase, K-feldspars and quartz.

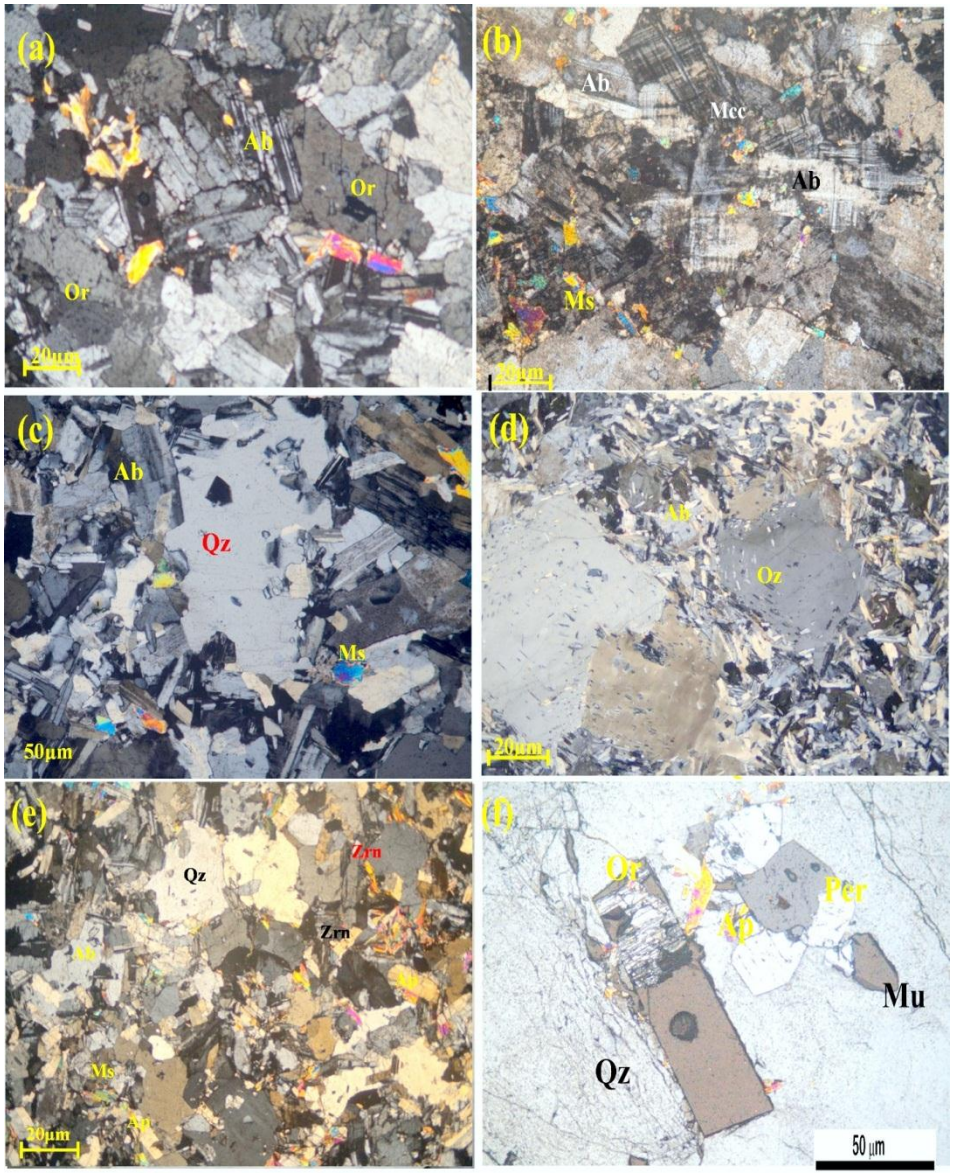


**Fig. 3.** Petrographical (Crossed nicols) features of Abu Dabbab albite granite showing (a) Orthoclase (Or) feldspar overgrown by albite (Ab) in albite granite. (b) Microcline (Mcc)) feldspar overgrown by albite (Ab) in the albite granite. (c) Albite crystals overgrown by quartz (Qz) with anhedral zircon (Zrn) in albite granite. (d) Snowball texture of quartz (Qz) in the porphyritic albite granite. (e) Albite (Ab), quartz (Qz), orthoclase (Or), muscovite (Ms), apatite (Apt) and zircon (Zrn) in albite granite. (f) Intergrown by apatite (Ap) and rutile (Rt) in the mineralized albite granite.

**Analytical methods**

Fourteen albite granite samples from Abu Dabbab were analyzed for major and trace elements to assess their geochemistry, magmatic affinity, and tectonic setting. Trace and rare earth elements, including Y, were measured at Central geochemical Labs of Complutense University, Madrid, Spain using a low-resolution quadrupole ICP-MS (NEX10N). Samples were digested via wet chemical methods using high-purity acids (HCl, $HNO_3$, HF) in PTFE vessels and processed through a series of heating, evaporation, and acid treatment steps. Solutions were then diluted and analyzed, employing an internal Ru-Rh-Re-Bi standard for matrix correction and instrumental drift. Procedural blanks and certified reference materials ensured data quality. Major oxides were determined via XRF, and geochemical modeling was performed using Igpet 2018 and Grapher 2017.

The Abu Dabbab albite granite samples were analyzed using X-ray diffraction (XRD) to determine their mineral assemblages at the Central Aanalytical Labs of Benha University. Powdered samples were prepared and examined on a Philips PW/1710 diffractometer equipped with a monochromator. The instrument operated with Cu Kα radiation ($\lambda = 1.54$ Å) at 40 kV and 35 mA, scanning over a 10°–90° 2θ range at a rate of 1° per second. Analyses also used nickel-filtered copper radiation ($\lambda = 1.54056$ Å) at settings of 45 kV and 40 mA. Peak identification and determination of interplanar spacings (d-spacings) were performed using the X' Pert High Score software.

**Mineral chemistry**

**Feldspar**

Electron microprobe data of plagioclase from ADG (Table 1and Fig.4a) confirm a composition close to pure albite ($An_{0–2}$), with only trace amounts of $K_2O$ (0.11–0.29 wt %) and $Ca_2O$ (< 0.02 wt %).

Electron microprobe analyses (Table 1; Fig. 4a) reveal that the K-feldspar in the ADG is compositionally consistent with orthoclase, containing 93–98 mol % Or and a minor albite component ($Na_2O$ = 0.14–0.46 wt %). This high Or content places it squarely in the orthoclase field—common in medium-temperature felsic plutonic rocks—and the slight $Na_2O$ impurity reflects limited albite incorporation. Such compositions are typical of alkali-feldspar varieties found in granitic intrusions

**Muscovite**

Electron microprobe results of muscovite (Table 2) reveal variable compositions: MgO ranges from 0.03 to 0.13 wt %, MnO from 1.01 to 2.11 wt %, $TiO_2$ is consistently below 0.24 wt %, and $Na_2O$ lies between 0.09 and 0.35 wt. %. The analysed muscovite samples of the ADG fall within magmatic muscovite field (Fig. 4b), where they are classified as Li-phengite which is indicative of Li-enriched that originated at late-stage magmatic conditions (Fig. 4c and d).

**Table 1: Electron microprobe analyses of the feldspars from the Abu Dabbab granite Centeral Eastern Desert, Egypt.**

| Rock type | Alkali feldspar granite | | | | | | | | | | | | | | | | | | | | | |
|---|---|---|---|---|---|---|---|---|---|---|---|---|---|---|---|---|---|---|---|---|---|---|
| Mineral | Alkali feldspar | | | | | | | | | | | | Plagioclase | | | | | | | | | |
| Sample | 125/g1 | | | 128/g1 | | | | 143/g1 | | | | | 125/g1 | | | 128/g1 | | | | 143/g1 | | |
| $SiO_2$ | 63.77 | 64.08 | 63.79 | 63.9 | 63.83 | 64.95 | 64.33 | 63.95 | 64.18 | 64.28 | 64.35 | | 68.16 | 67.74 | 68.06 | 69.12 | 67.8 | 67.8 | | 69.12 | 69.28 | |
| $Al_2O_3$ | 18.48 | 18.61 | 18.32 | 18.46 | 18.39 | 19.73 | 19.86 | 18.16 | 17.77 | 18.42 | 18.23 | | 19.24 | 18.92 | 19.34 | 19.43 | 19.38 | 18.85 | | 19.66 | 19.7 | |
| $FeO^t$ | 0.01 | 0.13 | 0.03 | 0.04 | 0.02 | 0.02 | 0.02 | 0.05 | 0.02 | 0.02 | 0.01 | | 0.03 | 0.11 | 0.01 | 0.02 | 0.05 | 0.06 | | 0.05 | 0.11 | |
| CaO | 0.01 | 0.02 | 0 | 0.01 | 0.01 | 0.04 | 0.01 | 0 | 0.01 | 0 | 0 | | 0.02 | 0.02 | 0.02 | 0.02 | 0.01 | 0.01 | | 0.01 | 0.01 | |
| $Na_2O$ | 0.39 | 0.25 | 0.46 | 0.22 | 0.14 | 0.32 | 0.23 | 0.37 | 0.24 | 0.34 | 0.33 | | 11.83 | 11.72 | 11.93 | 11.89 | 11.64 | 11.63 | | 11.81 | 11.71 | |
| $K_2O$ | 16.49 | 16.62 | 16.33 | 16.85 | 16.92 | 16.36 | 16.46 | 16.4 | 16.56 | 16.41 | 16.52 | | 0.09 | 0.1 | 0.14 | 0.14 | 0.21 | 0.2 | | 0.29 | 0.24 | |
| Total | 99.16 | 99.72 | 98.93 | 99.47 | 99.32 | 101.4 | 100.9 | 98.94 | 98.79 | 99.47 | 99.44 | | 99.37 | 98.61 | 99.5 | 100.6 | 99.09 | 98.55 | | 100.93 | 101.1 | |
| Cations based on 8 oxygens | | | | | | | | | | | | | | | | | | | | | | |
| Si | 2.98 | 2.98 | 2.99 | 2.98 | 2.98 | 2.96 | 2.95 | 2.99 | 3.01 | 2.99 | 3 | | 3 | 3 | 2.99 | 3 | 2.99 | 3.01 | | 2.99 | 3 | |
| Al | 1.02 | 1.02 | 1.01 | 1.02 | 1.01 | 1.06 | 1.07 | 1 | 0.98 | 1.01 | 1 | | 1 | 0.99 | 1 | 0.99 | 1.01 | 0.99 | | 1 | 1 | |
| $Fe^{3+}$ | 0 | 0.01 | 0 | 0.01 | 0.02 | 0.01 | 0 | 0 | 0 | 0 | 0 | | 0.01 | 0 | 0 | 0 | 0 | 0.01 | | 0 | 0.01 | |
| $Fe^{2+}$ | 0.01 | 0 | 0 | 0 | 0 | 0 | 0 | 0 | 0 | 0 | 0 | | 0 | 0 | 0 | 0 | 0 | 0 | | 0 | 0 | |
| Ca | 0 | 0 | 0 | 0 | 0 | 0 | 0 | 0 | 0 | 0 | 0 | | 0 | 0 | 0 | 0 | 0 | 0 | | 0 | 0 | |
| Na | 0.04 | 0.02 | 0.04 | 0.02 | 0.01 | 0.03 | 0.02 | 0.03 | 0.02 | 0.03 | 0.03 | | 1.01 | 1.01 | 1.02 | 1 | 1 | 1 | | 0.99 | 0.98 | |
| K | 0.98 | 0.99 | 0.98 | 1 | 1.01 | 0.95 | 0.96 | 0.98 | 0.99 | 0.97 | 0.98 | | 0.01 | 0.01 | 0.01 | 0.01 | 0.01 | 0.01 | | 0.02 | 0.01 | |
| Total | 5.02 | 5.02 | 5.02 | 5.03 | 5.03 | 5 | 5.01 | 5.01 | 5.01 | 5.01 | 5.01 | | 5.01 | 5.01 | 5.02 | 5.01 | 5.01 | 5.02 | | 5.01 | 5.01 | |
| End Members | | | | | | | | | | | | | | | | | | | | | | |
| An | 0.07 | 0.09 | 0.01 | 0.04 | 0.05 | 0.21 | 0.05 | 0.02 | 0.05 | 0 | 0 | | 0.1 | 0.09 | 0.07 | 0.09 | 0.04 | 0.06 | | 0.06 | 0.06 | |
| Ab | 3.48 | 2.26 | 4.13 | 1.91 | 1.28 | 2.84 | 2.07 | 3.31 | 2.18 | 3.07 | 2.91 | | 99.4 | 99.38 | 99.14 | 99.15 | 98.8 | 98.8 | | 98.37 | 98.62 | |
| Or | 96.45 | 97.65 | 95.85 | 98.05 | 98.67 | 96.89 | 97.85 | 96.67 | 97.78 | 96.92 | 97.09 | | 0.5 | 0.54 | 0.79 | 0.76 | 1.16 | 1.12 | | 1.57 | 1.32 | |

**Table 2: Electron microprobe analyses of the muscovite from the studied Abu Dabbab granite, Central Eastern Desert, Egypt.**

| Mineral | Muscovite | | | | | | | | |
|---|---|---|---|---|---|---|---|---|---|
| Rock type | Alkali feldspar granite | | | | | | | | |
| Sample | 125/g1 | | 128/g1 | | | 143/g1 | | | |
| $SiO_2$ | 43.90 | 43.18 | 42.38 | 43.16 | 42.56 | 44.05 | 43.41 | 46.49 | 46.68 |
| $TiO_2$ | 0.22 | 0.21 | 0.08 | 0.24 | 0.17 | 0.07 | 0.10 | 0.11 | 0.12 |
| $Al_2O_3$ | 20.44 | 19.96 | 20.48 | 20.05 | 19.32 | 21.06 | 21.56 | 26.57 | 26.39 |
| FeO | 14.74 | 15.76 | 16.11 | 16.00 | 15.34 | 14.07 | 15.07 | 8.88 | 8.83 |
| MnO | 2.11 | 2.04 | 1.71 | 1.22 | 1.65 | 1.83 | 1.91 | 1.01 | 1.01 |
| MgO | 0.05 | 0.03 | 0.06 | 0.05 | 0.05 | 0.11 | 0.12 | 0.13 | 0.12 |
| CaO | 0.00 | 0.02 | 0.00 | 0.01 | 0.00 | 0.01 | 0.02 | 0.00 | 0.03 |
| $Na_2O$ | 0.18 | 0.11 | 0.11 | 0.13 | 0.11 | 0.10 | 0.09 | 0.29 | 0.35 |
| $K_2O$ | 10.12 | 10.07 | 9.94 | 10.10 | 10.23 | 10.12 | 10.01 | 10.39 | 10.41 |
| Li2O* | 2.27 | 2.21 | 2.29 | 1.78 | 1.73 | 1.00 | Li2O* | 2.38 | 2.27 |
| F | 7.90 | 7.54 | 7.35 | 7.41 | 7.61 | 5.96 | 5.80 | 3.37 | 3.46 |
| Cl | 0.00 | 0.01 | 0.01 | 0.00 | 0.00 | 0.01 | 0.00 | 0.00 | 0.04 |
| H2O* | 0.34 | 0.46 | 0.52 | 0.51 | 0.34 | 1.23 | 1.32 | 2.69 | 2.64 |
| Subtotal | 100.00 | 99.39 | 98.74 | 98.86 | 97.40 | 98.62 | 99.41 | 99.92 | 100.10 |
| O=F,Cl | 8.24 | 8.01 | 7.88 | 7.92 | 7.96 | 7.21 | 7.13 | 6.06 | 6.15 |
| Total | 91.76 | 91.38 | 90.86 | 90.94 | 89.44 | 91.41 | 92.28 | 93.85 | 93.95 |
| | Cations based on 22 oxygens | | | | | | | | |
| Si | 6.44 | 6.42 | 6.34 | 6.43 | 6.45 | 6.50 | 6.39 | 6.49 | 6.51 |
| $Al^{IV}$ | 1.56 | 1.58 | 1.66 | 1.57 | 1.55 | 1.50 | 1.61 | 1.51 | 1.49 |
| $Al^{VI}$ | 1.98 | 1.91 | 1.96 | 1.95 | 1.91 | 2.16 | 2.13 | 2.87 | 2.85 |
| Ti | 0.02 | 0.02 | 0.01 | 0.03 | 0.02 | 0.01 | 0.01 | 0.01 | 0.01 |
| $Fe^{2+}$ | 1.81 | 1.96 | 2.02 | 1.99 | 1.95 | 1.74 | 1.86 | 1.04 | 1.03 |
| Mn | 0.26 | 0.26 | 0.22 | 0.15 | 0.21 | 0.23 | 0.24 | 0.12 | 0.12 |
| Mg | 0.01 | 0.01 | 0.01 | 0.01 | 0.01 | 0.03 | 0.03 | 0.03 | 0.03 |
| Ca | 0.00 | 0.00 | 0.00 | 0.00 | 0.00 | 0.00 | 0.00 | 0.00 | 0.00 |
| Na | 0.05 | 0.03 | 0.03 | 0.04 | 0.03 | 0.03 | 0.03 | 0.08 | 0.09 |
| K | 1.89 | 1.91 | 1.90 | 1.92 | 1.98 | 1.91 | 1.88 | 1.85 | 1.85 |
| OH* | 0.33 | 0.45 | 0.52 | 0.51 | 0.35 | 1.21 | 1.30 | 2.51 | 2.46 |
| Li* | 1.36 | 1.33 | 1.40 | 1.06 | 1.02 | 0.56 | Li* | 1.41 | 1.36 |
| F | 3.67 | 3.54 | 3.48 | 3.49 | 3.65 | 2.78 | 2.70 | 1.49 | 1.53 |
| Cl | 0.00 | 0.00 | 0.00 | 0.00 | 0.00 | 0.00 | 0.00 | 0.00 | 0.01 |
| Total | 18.03 | 18.10 | 18.14 | 18.09 | 18.10 | 18.10 | 18.17 | 17.99 | 17.99 |
| Mg# | 0.01 | 0.00 | 0.01 | 0.01 | 0.01 | 0.01 | 0.01 | 0.02 | 0.02 |
| $Al^{Total}$ | 3.54 | 3.50 | 3.61 | 3.52 | 3.45 | 3.66 | 3.74 | 4.38 | 4.34 |

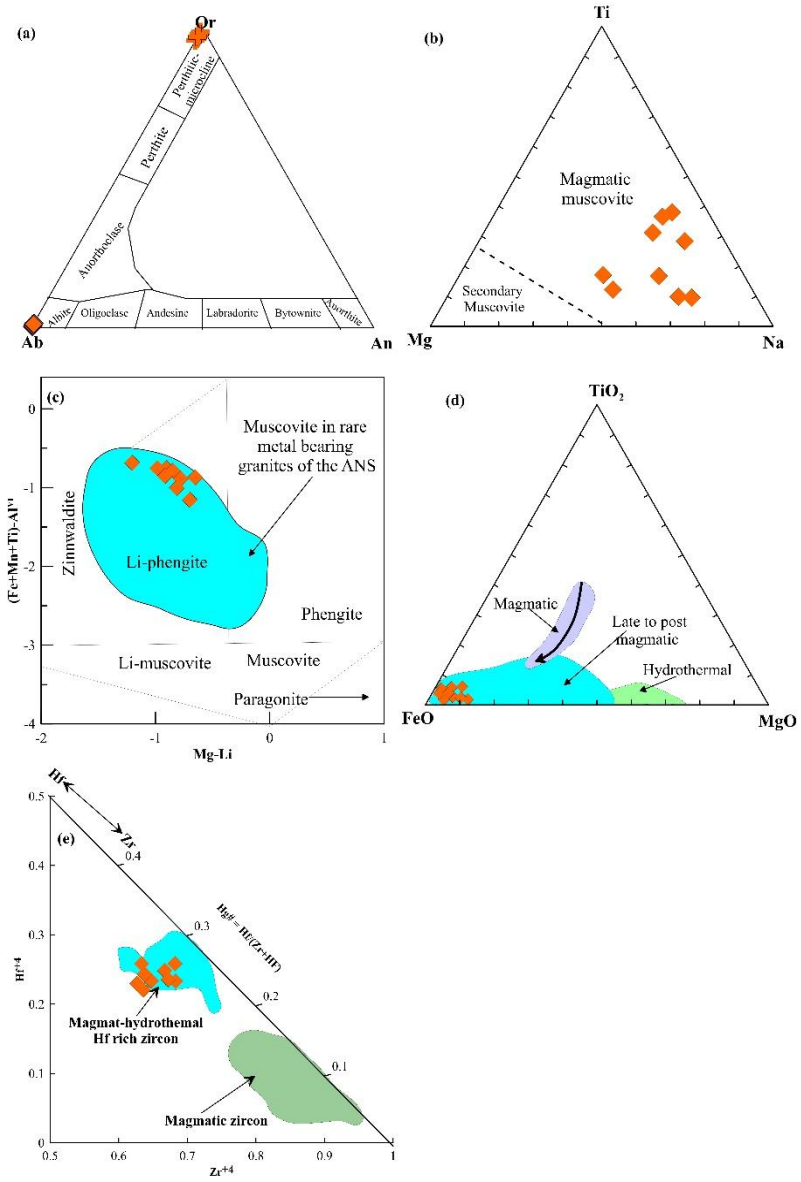


**Fig. 4.** Mineral chemistry of feldspar and muscovite and zircon from ADG. (a) Feldspar classification diagram of the AKAG **(Deer, *et al.*, 1992)**. (b) Geochemical discrimination diagrams of primary and secondary muscovite, geochemical field are after **Sun, *et al.*, (2002).** (c), (d) classification of muscovite composition from the ADG evaluated using a classification diagrams Mg–Li against $(Fe + Mn + Ti) – Al^{iv}$ after **(Tischendorf, *et al.*, 1997)**. (d) TiO2−FeO−MgO diagram after **(Monier, *et al.*, 1984)**. (e) Zr vs. Hf scatter plot for zircon grains field after **(Zhu *et al.*, 2002)**.

**Zircon**

High Hf concentrations and low Zr/Hf ratios in zircon are well-known indicators of late-stage or hydrothermal overgrowth in highly fractionated granite systems. Experimental results show that late-crystallizing zircons—and especially hydrothermal varieties—tend to have elevated $HfO_2$ and reduced Zr/Hf, reflecting evolving $D_{ho}$ values as temperatures decline **(Wang *et al.*, 2010)**. Such features align with enrichment trends observed in peralkaline to rare-metal granites, where pronounced Hf-rich rims form around earlier zircon cores **(Breiter *et al.*, 2024).**

Accordingly, the ADG zircons (Table 3) likely record a magmatic history transitioning into hydrothermal conditions, preceded by zircon crystallization during advanced melt differentiation and later modified by fluid-driven processes in a metal-rich environment (Fig. 4e).

**Bulk mineralogy using X-Ray Diffraction (XRD)**

Six surface samples of ADAG were selected for X-ray diffraction technique to identify and determine their mineralogical compositions.

The corresponding spectrums of the studied albite granite are shown in Figures 5a and b as well as the analyzed results are recorded in Table (4). X-Ray Diffraction analysis of the studied albite granite revealed that some rare earth elements and other rare metals-bearing minerals such as Fe–tapiolite, pyrochlore, tantalite-Mn, cassiterite, eudialyte, zircon, ixiolite, gadolinite-Y, yattria, bastnasite, xenotime, euxenite-Y, allanite-Nd, paracite-Ce, monazite-Nd, thorite and thorianite.

Scanning Electron Microscopy and energy dispersive spectroscopy (SEM/EDX) analysis of the heavy minerals of the studied albite granite revealed that columbite-Mn-Tantalite-Mn, pyrochlore, cassiterite, zircon, xenotime, euxenite, loparite-Ce, gadolinite-Y, monazite-Nd, samarkite-Yb and tapiolite and thorite are the dominance of minerals in studied albite granite (Fig. 5c).

Based on compiling extremely specific elemental composition data across an area of a sample elemental mapping is done using Scanning Electronic Microscope to identify the distribution and concentration of elements in each sample.

Elemental mapping of the studied albite granite showed that the high field strength elements (e.g: Ta, Nb, Hf and Zr), rare earth elements (e.g: Dy, Ho, Yb Lu, Y and Er), transition metals (e.g: Sn, Fe, Ti and Mn) and radioactive elements (e.g: Th and U) are prevalent in the studied albite granite in a large proportion than the other elements. In addition, the concentrations of analyzed samples are calculated by using ArcGIS Map to show the distribution of the rare earth elements and rare metals in Abu Dabbab albite granite. Figure (6a) displays the concentration of light rare earth elements occupy the SE part of granite pluton. Where Figure (6b) defines the concentration of heavy rare earth elements in the NW, NE and SE parts of the Abu Dabbab granite. Figure (6c) shows the concentration of the other rare metals in the NE and N parts of the ADG.

**Table 3: Electron microprobe analyses of the Zircon from the studied Abu Dabbab granite, Central Eastern Desert, Egypt.**

| Mineral | Zircon | | | | | | | | |
|---|---|---|---|---|---|---|---|---|---|
| Rock type | Alkali feldspar granite | | | | | | | | |
| Sample | 125/g1 | | 128/g1 | | | 143/g1 | | | |
| SiO2 | 30.35 | 28.89 | 29.89 | 30.18 | 30.07 | 29.63 | 29.54 | 28.13 | 29.31 |
| ZrO2 | 37.42 | 40.25 | 40.64 | 39.85 | 40.03 | 38.62 | 38.52 | 39.95 | 37.91 |
| HfO2 | 26.56 | 25.85 | 23.27 | 24.39 | 24.78 | 23.91 | 22.84 | 23.62 | 24.34 |
| ThO2 | 0.04 | 0.03 | 0.03 | 0.04 | 0.03 | 0.56 | 0.63 | 0.54 | 0.52 |
| UO2 | 1.47 | 0.98 | 1.17 | 1.23 | 1.27 | 1.64 | 2.32 | 1.97 | 2.06 |
| Y2O3 | 0.01 | 0.01 | 0.01 | 0.01 | 0.01 | 0.03 | 0.35 | 0.31 | 0.35 |
| FeO | 0.03 | 0.04 | 0.04 | 0.03 | 0.05 | 0.22 | 0.26 | 0.25 | 0.27 |
| MnO | 0.02 | 0.02 | 0.03 | 0.01 | 0.02 | 0.01 | 0.02 | 0.01 | 0.02 |
| CaO | 0.001 | 0.007 | 0.004 | 0.001 | 0.009 | 2 | 1.64 | 1.4 | 1.59 |
| P2O5 | 0.15 | 0.21 | 0.11 | 0.16 | 0.18 | 1.13 | 1.67 | 1.43 | 1.46 |
| Al2O3 | 1.36 | 1.09 | 1.25 | 1.69 | 1.17 | 1.19 | 2.44 | 0.7 | 0.81 |
| TiO2 | 0.03 | 0.02 | 0.04 | 0.02 | 0.02 | 0.02 | 0.07 | 0.04 | 0.06 |
| H2O* | 97.44 | 97.4 | 96.48 | 97.61 | 97.64 | 97.75 | 97.8 | 97.61 | 97.83 |
| Total | 30.35 | 28.89 | 29.89 | 30.18 | 30.07 | 29.63 | 29.54 | 28.13 | 29.31 |
| | Cations based on 4 oxygens | | | | | | | | |
| Si4+ | 1.048 | 1.0075 | 1.0325 | 1.0309 | 1.0329 | 1.0008 | 0.9747 | 0.9691 | 0.9979 |
| Zr4+ | 0.63 | 0.6844 | 0.6845 | 0.6637 | 0.6704 | 0.6358 | 0.6197 | 0.6711 | 0.6294 |
| Hf4+ | 0.2618 | 0.2573 | 0.2294 | 0.2378 | 0.2429 | 0.2305 | 0.2152 | 0.2323 | 0.2366 |
| Th4+ | 0.0003 | 0.0002 | 0.0002 | 0.0003 | 0.0002 | 0.0043 | 0.0047 | 0.0043 | 0.0041 |
| U4+ | 0.0113 | 0.0076 | 0.009 | 0.0093 | 0.0097 | 0.0123 | 0.017 | 0.0151 | 0.0156 |
| Y3+ | 0.0002 | 0.0002 | 0.0002 | 0.0002 | 0.0002 | 0.0005 | 0.0062 | 0.0056 | 0.0063 |
| Fe2+ | 0.0009 | 0.0012 | 0.0012 | 0.0009 | 0.0014 | 0.0062 | 0.0073 | 0.0071 | 0.0077 |
| Mn2+ | 0.0005 | 0.0005 | 0.0007 | 0.0002 | 0.0005 | 0.0002 | 0.0004 | 0.0002 | 0.0004 |
| Ca2+ | 0 | 0.0003 | 0.0001 | 0 | 0.0003 | 0.0723 | 0.0581 | 0.0518 | 0.0581 |
| P5+ | 0.0044 | 0.0062 | 0.0032 | 0.0046 | 0.0052 | 0.0324 | 0.0467 | 0.0417 | 0.0422 |
| Total | 2.013 | 2.011 | 2.013 | 2.016 | 2.012 | 2.043 | 2.046 | 2.028 | 2.032 |
| Zr/Hf | 2.41 | 2.66 | 2.98 | 2.79 | 2.76 | 2.76 | 2.88 | 2.89 | 2.66 |
| Th/U | 0.03 | 0.03 | 0.03 | 0.03 | 0.02 | 0.35 | 0.28 | 0.28 | 0.26 |
| Hf/(Hf+Zr) | 0.29 | 0.27 | 0.25 | 0.26 | 0.27 | 0.27 | 0.26 | 0.26 | 0.27 |

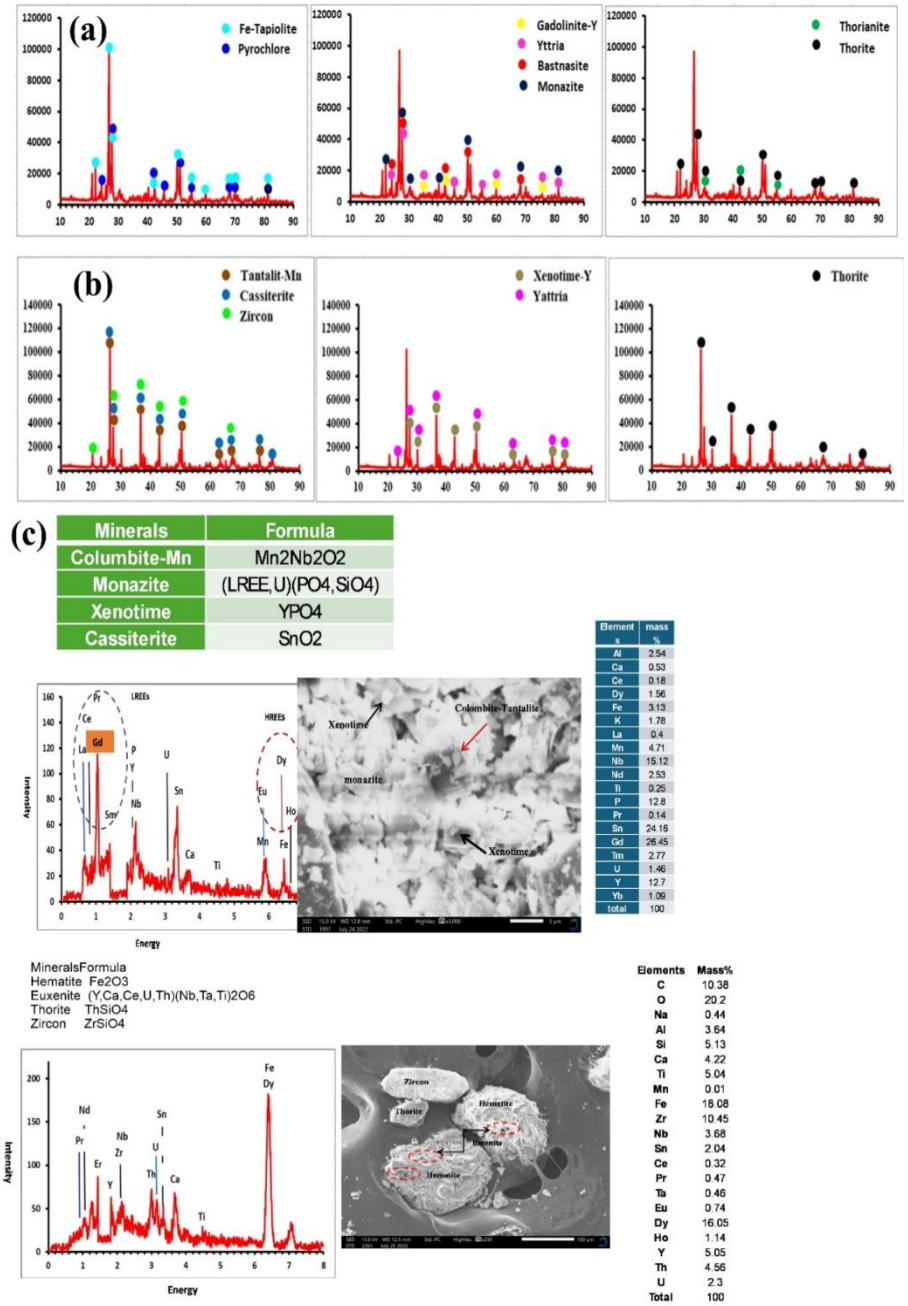


**Fig. 5.** (a, b) X-Ray Diffraction pattern showing the identified minerals of the studied albite granite (mineral names are embedded in the figures. (c) SEM Images and EDX analysis of different minerals within Abu Dabbab granites (mineral`s name and formulae are embedded in figures)

**(c)**

**Tantalite-Mn; Loparite-Ce; Samarkite- Yb**

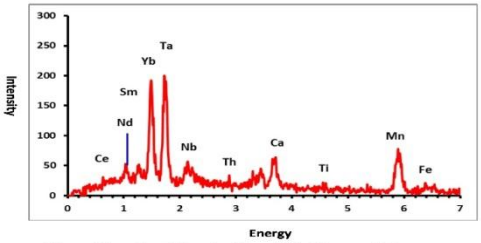


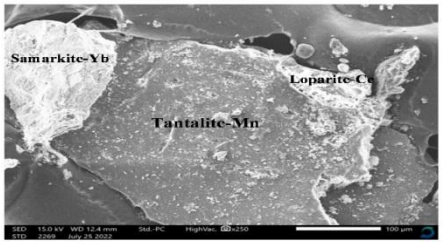


Cassiterite; Tantalite-M; Pyrochlore

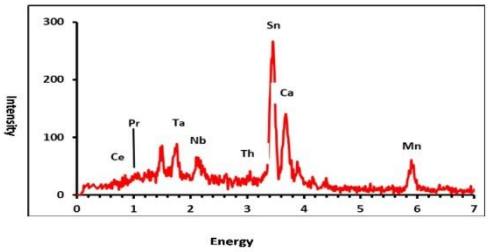


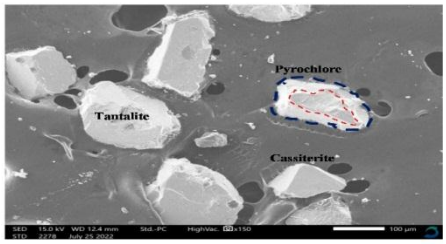


Tantalite-Mn

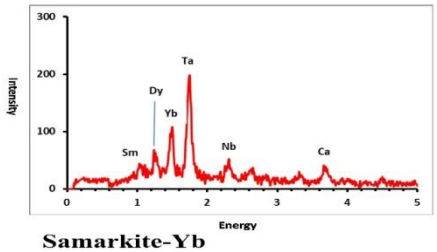


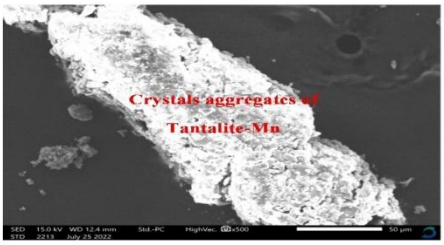


**Samarkite-Yb**

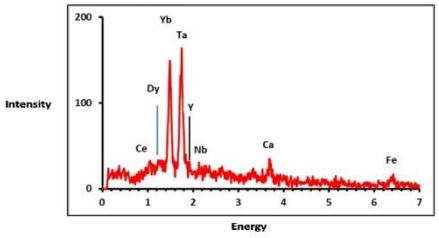


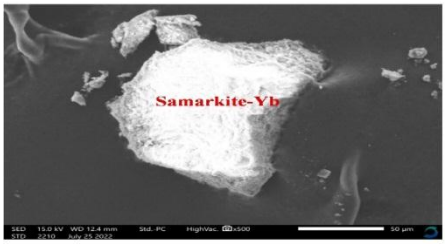


**Malachite; Gadolinite-Y; Monazite**

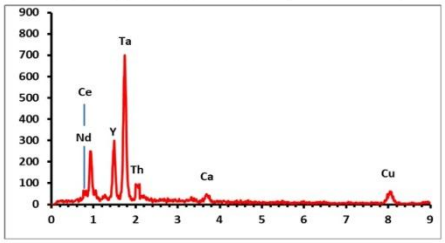


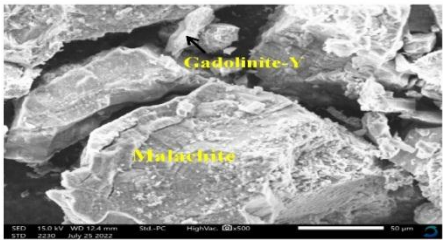


**Fig. 5. Continued**

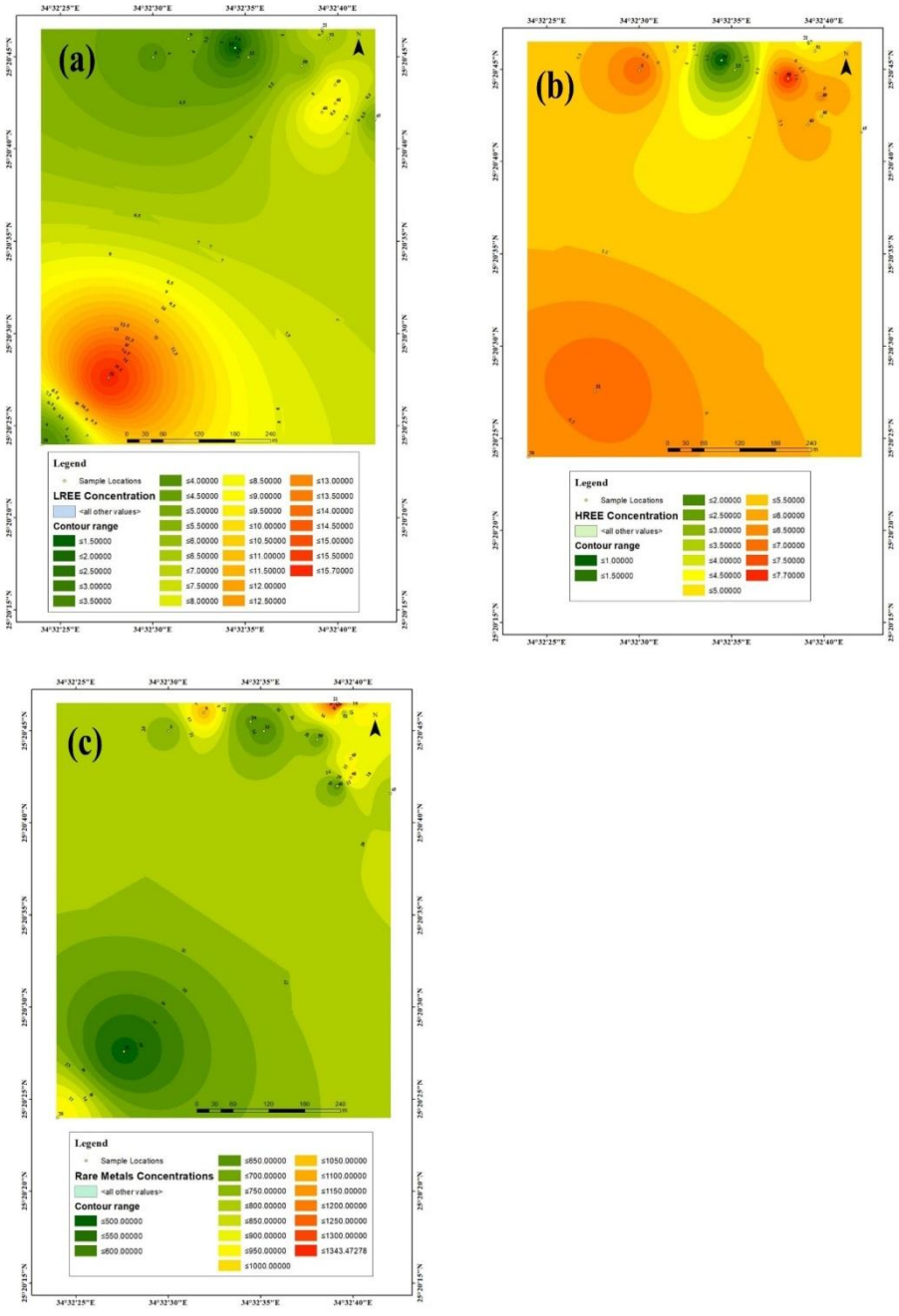


**Fig. 6.** Distribution maps of the (a) light rare earth elements; (b) heavy rare earth elements and (c) rare metals of the Abu Dabbab albite granite.

**Table 4: Phases data view of X-Ray Diffractogram of the studied albite granite.**

| Phases | Chemical formula | 2Θ | d, Å |
|---|---|---|---|
| Thorianite | $ThO_2$ | 27.5,31.9,45.8,54.3,56.9, 66.8,73.7,76,84.8 | 3.23,2.79,1.97,1.68,1.61,1.39, 1.28, 1.25, 1.14 |
| Thorite | (Th,U) $SiO_4$ | 25,31.3,40.5,51.5,55,67.3,69.1, 70.1, 81.2 | 3.55,2.84, 2.22,1.76,1.77,1.66,1.38,1.34,1.34,1,18 |
| Fe-tapiolite | $(Fe,Mn)(Nb,Ta)_2O_6$ | 26,27,28,43,50,55,60.2, 68.3,70.60,81 | 4.14,3.29,3.09,2.08,1.71,1.64,1.53,1.37,1.33,1.17 |
| Parisite-Ce | $Ca\ (Ce,La)_2(CO_3)_3F_2$ | 24.4,30.3,40,50,68 | 3.46,2.94,2.24,1.82,1.37 |
| Loparite-Ce | $(Ce,Na,Ca)\ (Ti,Nb)O_3$ | 40.9,46,69.7,74.6 | 2.20,1.90,1.34,1.27 |
| Monazite-Nd | (Ce,La,Nd,Th) $(PO_4,SiO_4)$ | 21.2,26.5,27.2,30.1,40.3,50.5,51.5,68.5,69.4,81.2 | 4.17,3.36,3.20,3.15,2.95,2.23,1.80,1.80,178,1.36,1.35,1.19 |
| Allanite-Nd | (Ca,Ce,La,Nd,Th) $(Fe,Al)Si_3O_{12}(OH)$ | 22.1,24.9,30.5,40.7,50.9,76,81 | 4.01,3.56,2.92,2.20,1.85,1.25,1.18 |
| Bastanasite | $(Ce,La,Y)\ CO_3F$ | 22.1,27,40.1,50,4,68 | 1.82,1.76,1.53,1.22,1.03 |
| Tantalite-Mn | $Mn\ TaO_6$ | 13.4,24,26,35,36,49.9,50,54,63,64,77,81.3,89.9 | 7.28,3.64,3.34,2.44,1.82,1.82,1.68,1.47,1.54,1.23,1.18,1.09 |
| Gadolinite-Y | $(LREE,Nd)_2$ $FeBe_2Si_2O_{10}$ | 21.9,35.1,43.2,59,63,77, 81, 89.8 | 4.04,2.55,2.09,1.56,1.47,1.23,1.19,1.09 |
| Ixiolite | $(Ta,Nb,Sn,Mn,Fe)_4O_8$ | 28.8,35.6,39.9,44.7,54.9,60.3,67.2,73.1,80.4 | 2.98,2.51,2.25,2.02,1.66,1.53,1.39,1.29,1.19 |
| Yttria | $YO_2$ | 23.7,29.2,36,39.9,47,54.8,60,6,66,73.8,80.1 | 3.73,3.05,2.49,2.25,1.92,1.67,1.52,1.41,1.28,1.19 |
| Cassiterite | $SnO_2$ | 26.2,37.4,38.9,42.1,51.1,61,68.3,70.3,73.4,77.6, 82.5 | 3.39,2.39,2.33,2.14,1.78,1.51,1.37,1.33,1.28,1.22,1.16 |
| Euxinite | (Ca,Ce,U,Th,Y) $(Nb,Ta,Ti)_2O_6$ | 24.3,26.6,30,38.8,49.9,58.6,67.1,77,81 | 3.65,3.34,2.97,2.31,1.82,1.57,1.39,1.23,1.18 |
| pyrochlore | $(Na,Ca)_2Nb_2O_6(OH,F)$ | 24,28.2,42.3,45,55.5,66.9,77.3,82.4 | 3.69,3.15,2.13,2.o1,1.65,1.39,1.23,1.16 |
| Xenotime | $YPO_4$ | 26.2,37.4,39.3,42.4,50.6,62.3,68.8,77.1,79.8 | 3.39,2.40,2.28,12.2,1.80,1.48,1.36,1.23,1.20 |
| Zircon | $ZrSiO_4$ | 20.2,27,36.1,38.6,43.9,63,68.3 | 4.37,3.29,2.47,2.05,1.47,1.37 |

**Whole-rock major and trace element compositions**

Results of the chemical analyses for the studied gneissose granite rocks are shown in Table 5. The ADG are geochemically characterized by their significant homogeneity in terms of both major and trace element geochemistry, therefore they exhibit a narrow range of chemical composition. ADG is characterized by enrichment of $SiO_2$ (70.89-76.6 wt. %), $Al_2O_3$ (13.44–16.22 wt. %), $Na_2O$ (4.45-7.25 wt. %), $K_2O$ (2.19- 7.25) and depletion of MgO (03-1.05 wt.%), CaO (0.03-1.11wt. %), $TiO_2$ (0.03-1.04 wt.%), FeO (0.16-1.27 wt.%) and $P_2O_5$ (0.05-1.07 wt. %; Table 5).

According to normative mineral calculations, the ADG plot predominantly in the alkali feldspar granite field (Fig. 7a), in full agreement with petrographic observations. Geochemically, they closely resemble Egyptian younger granites (Fig. 7b). These samples display high $K_2O/Na_2O$ ratios (1.09–1.63), clearly pertaining to medium- to high-potassium series (Fig. 7c).

The relatively high $Al_2O_3$ contents of ADG resulting in slightly peraluminous affinity, where most of ADG samples possess A/CNK >1 (Fig. 7d). This is corroborated by the presence of normative corundum up to 3.56 the occurrences of primary muscovite in all samples (Figs. 3 and 4). Moreover, ADG possess high contents of total alkali ($Na3_2O$ + $K_2O$ = 7.98–11.21 wt.%) produce elevated agpaitic indices (AI = (Na + K)/Al ≈ 0.67–0.96), suggesting a mildly alkaline affinity **(Liegeois *et al.*, 1998)**, similar to other Pan-African A-type granites **(Abuamarah *et al.*, 2021).** Moreover, the plots normative components of ADB indicated that their melts temperature (~670$^o$-800$^o$), while the pressure isobars indicate formation under pressures varying between 1-4 kb (Fig. 7e). In addition their low MgO (0.03–0.15 wt. %) and moderate FeOt (0.16–0.91 wt %) yield low Mg# values (7.84-23.08), alongside high Fe-number (Fe# = FeOt/(FeOt + MgO)), classify the ADG as ferroan A-type granite (Fig. 6f), which is the typical characteristics of anorogenic, post-collisional igneous rocks of the ANS **( Azer *et al.*, 2023; Feteha *et al.*, 2022and Lashin *et al.*, 2023)**.

Trace-element abundances of ADG display enrichments in large-ion lithophile elements (LILE, e.g., Rb, Cs) and certain high-field-strength elements (HFSE; Y, Nb, Ta, U, Sc), while Ba, Sr, Eu and Ti remain comparatively low. Moreover, the negative correlation between $Na_2O$ and $K_2O$ (Table 5) aligns with trends typical of low-Ca granites. Silica correlates positively with alkalis and negatively with most other oxides, reflecting strong magmatic fractionation trends (Fig. 8).

Whole-rock rare-earth element (REE) data with elemental ratios are provided in Table 5, while Figure 9a displays chondrite-normalized REE patterns. The albite granite exhibits elevated heavy rare-earth

element (HREE) concentrations compared to light rare-earth elements (LREE), along with strongly negative europium anomalies and markedly low Ba (3.61.58.92 ppm) and Sr (40.28-71.18 ppm) levels. These characteristics represent typical of melts that are residues from extensive feldspar removal through magmatic differentiation, under moderate to reducing conditions where $Eu^{2+}$ is stabilized **(Hanson, 1978 ; Möller and Muecke, 1984 ; Azer, 2013 and Lee *et al.*, 2013;)**. Although Sr, Ba, and Ca are fluid-mobile and could be affected during late-stage fluid alteration—leading to strong negative Eu anomalies—the absence of direct correlations between Eu and these elements suggests that the anomalies primarily result from feldspar fractionation rather than fluid mobilization. Chondrite-normalized REE profiles display a clear "M-type" tetrad effect: a convex upward segmentation into four REE groups (La–Nd; Pm–Gd; Gd–Ho; Er–Lu), consistent with highly evolved, fluorine-rich intrusive systems **(Macdonald *et al.*, 1987)**.

Primitive mantle-normalized multi-element diagrams of ADG (Fig. 9b) displays strong positive anomalies in Rb, Th, U, and especially Ta, while showing deep negative troughs in Ba, Sr, P, and Ti. Significantly, the Rb/Sr ratios exceed 20 (ranging from 21 to 204), whereas Nb/Ta and Zr/Hf ratios are exceptionally low at 0.44–0.60 and 1.89–2.38, respectively. These signatures closely resemble those found in peraluminous, rare-metal–enriched granites of the Arabian–Nubian Shield **(Azer *et al.*, 2019b; Azer *et al.*, 2023 and El Hadek *et al.*, 2016)**. The concurrent negative anomalies in Ba, Sr, La, Ce, Eu, and Ti resemble patterns seen in both peralkaline A-type granites **(Platt & Woolley, 1986; Macdonald *et al.*, 1987 and Abdel-Rahman, 2006)** and strongly fractionated I-type granites **(Champion and Chappell, 1992)**.

**Albite granite vs. albitized granite**

Most ADG samples display very low loss-on-ignition values (<1.5 %), indicating minimal alteration. No strong correlation exists between LOI and alkali content ($Na_2O$, $K_2O$; Figs. 10a and b), which further suggests these rocks have remained largely unaltered. Chemical Index of Alteration (CIA) values range from 50.27 to 54.89, consistent with unweathered felsic rocks (CIA ≈ 45–55), pointing to weak chemical weathering **(Nesbitt and Young, 1982)**. However, ADG samples contain albite-rich plagioclase and low CaO, which could be predicted for albite metasomatism **(King *et al.*, 1997)**, their high ΣREE and moderate Zr content argue against significant albitization **(Zaraisky *et al.*, 2009)**. Additionally, the positive Sr–Ca correlation reinforces the absence of fluid-driven albite replacement **(Castorina *et al.*, 2006 and He *et al.*, 2021)**. During albitization, Sr can be mobilized

and redistributed, leading to changes in its concentration and isotopic ratios within the rock **(He *et al.*, 2021)**, thus if albitization had occurred, it is expected for Sr to deviate from its original geochemical trend due to its mobility during the alteration **(Castorina *et al.*, 2006)**. Regarding to ADG, Sr exhibit positive correlation with CaO (Fig. 10c), which refuting the possibility of albite metasomatism. Accordingly, we can suggested that the studied granite rocks are albite granites not albitized granites, where the rematked excess of albite are attributed to the magmatic process rather rhan hydrotherma enrichements.

**Petrological Classification & Magmatic Evolution**

The typology of ADG has been controversial, in that they were previously classified as I-type granite type **(Heikal *et al.*, 2019 ; Abuamarah *et al.*, 2021 and Moussa *et al.*, 2021)**, however, the analysed sample of ADG are characterized by high $K_2O/Na_2O$ and $K_2O/MgO$ ratios with high molar $FeO^t/(FeO^t+MgO)$ with low CaO and MgO (Table 5), which represent the typical characteristics of highly fractionated A-type granitoids **(Collins *et al.*, 1982; Creaser *et al.*, 1991 and Bonin, 2007)**. Moreover, ADG display classic characteristics of high-K calc-alkaline suites (Fig. 6c). Their mildly peraluminous compositions (A/CNK ≈ 0.99–1.05; Fig. 6d) and dominaant orthoclase, plagioclase, quartz, and muscovite, with decreasing $Al_2O_3$, MgO, $Fe_2O_3$, CaO, $TiO_2$, and $P_2O_5$ as $SiO_2$ increases (Fig. 8), marked by depleted Zr and Hf and strong negative Eu anomalies (Fig. 9b) are significant characterstics of Highly Evolved Granites (HEGs) **(Jahn *et al.*, 2001 and Wu *et al.*, 2003)**.

**Petrogenesis of the ADG**

Two main petrogenetic scenarios often explain highly evolved granites: extensive fractional crystallization and partial melting of metasedimentary or meta-igneous sources **(Li *et al.*, 2007; Zhao and Deng, 2016 and Wu *et al.*, 2017)**. The ADG are charcterized by markedly high Rb and low Sr/Ba levels, along with $Rb/Sr > 2.9$, $Rb/Ba > 0.93$, $K/Ba > 13$, and $Eu/Eu^* < 0.35$—point to dominant crystal fractionation, especially of K-feldspar and plagioclase.

The majority of ADG samples have low Nb/Ta (0.21-1.02) and Zr/Hf (0.63-3.11) ratios consistent with typical highly evolved granites, such as the Nuweibi, Um Dargag and Um Maiat granites from the South Eastern Desert, Egypt **(Moussa *et al.*, 2021)**. The pronounced negative P anomalies (Fig. 9b) reflecting the fractionation of apatite and/or of the ADG parental magma, whereas the depletion of Ti requires an advanced degree of ilmenite and/or titanomagnetite fractionation at upper crustal levels. Moreover, ADG samples possess pronounced negative anomalies of Ba, Sr, La, Ce, Eu and Ti resembling peralkaline A-type

granites (e.g., **Woolley, 1986 ; Macdonald *et al.*, 1987 and Platt and Abdel-Rahman, 2006 )**

**Ballouard *et al.* (2016)** delineated four primary categories of rare-metal-rich felsic magmas: (1) muscovite-dominated peraluminous granites (MPG) , (2) $A_1$ -type intraplate granites, (3) $A_2$ -type late-orogenic granites and associated syenites, and (4) felsic rocks that are undersaturated in silica. The ADG clearly belongs to the MPG category—it hosts abundant muscovite and disseminated Ta–Nb–Sn minerals such as cassiterite, columbite–tantalite group minerals. It is distinguished by its peraluminous chemistry (A/CNK > 1), very low $P_2O_5$ concentrations, and extremely low Nb/Ta ratios (0.21-1.02), clearly matching the geochemical fingerprint of highly peraluminous, rare-metal pegmatitic granites (Figure 10d).

Muscovite-rich peraluminous granites (MPGs), such as ADG, are inferred to originate through one of two main processes: either extensive fractional crystallization of mafic magmas ascending from the mantle, or dehydration melting of mica-bearing crustal materials—such as sedimentary rocks or igneous crust—under collisional or late-collisional tectonic conditions.

The ADG exhibits pronounced sensitivity to magmatic differentiation. Primitive mantle–normalized trace-element profiles (Fig. 9b) reveal strong enrichments in Rb, Th, U, and Ta and deep depletions in Ba, Sr, P, and Ti. The ADG display exceptionally high Rb/Sr ratios (21–204), extremely low Nb/Ta ratios (0.44–0.60), and low Zr/Hf ratios (1.89–2.38). These characteristics closely resemble those found in peraluminous rare–metal granites of the Arabian–Nubian Shield and low P–Ta granites worldwide **(Wang *et al.*, 2023)**. Moreover,

In Abu Dabbab, the peraluminous composition, elevated $SiO_2$, and low MgO, FeO, Co, and Ni contents refute a mantle-derived origin. Coupled with very high Rb/Sr ratios and Th/U values (~1.4–2.9) similar to continental crust (Th/U ≈3.8), it becomes clear that crustal melting, rather than fractionating a mantle basalt, generated these magmas.

The geochemical characteristics of the ADG clearly reflect extensive fractional crystallization of feldspar minerals under the influence of fluorine-rich magmatic fluids. The mildy peraluminous affinity, with elevated total alkalis ($K_2O + Na_2O$), and strong depletion of Ba, Sr, P, Eu, and Ti relative to primitive mantle values (Figure 9b), regarded as the main charcterstics of the ADG. In addition, the marked negative anomalies in Ba, Sr, and Eu indicate substantial removal of albite and K-feldspar from the melt. Albite fractionation depletes Sr and Eu, while removal of K-feldspar also results in Ba and Sr depletion. Morover, The pronounced depletion in Sr and Eu within the ADG

strongly indicates a prolonged sequence of feldspar crystallization **(Zhu *et al.*, 2002)**, with both plagioclase and alkali feldspar being systematically removed from the melt. This is further supported by trends observed in geochemical plots—specifically Sr vs. Ba and Sr vs. Rb/Ba (Figure 10e, f), which trace the evolving melt chemistry. These plots clearly show Sr decreasing in tandem with increasing ratios of Rb/Ba, consistent with fractional removal first of plagioclase (which extracts Sr and Eu) followed by K-feldspar (which consumes Ba and additional Sr). Such multi-element covariations are classic indicators of sequential feldspar fractionation during magmatic evolution. Furthemore, ADG samples are aligned along a linear trend characteristic of high-silica granites (Fig. 10f), which are proposed to be the residual liquids formed after extensive fractional crystallization of a felsic parent melt residual liquids after extreme fractional crystallisation of a felsic parent melt ( **Xiao *et al.*, 2023**). This is evidenced by higher $K_2O$ and Rb contents than those of high silica granite, plus good correlation between Nb/Ta with Zr/HF (e.g. Peninsular Range batholith; Figs. 13b-d). In addition, many authors have recorded floutite within ADG **( Sami *et al.*, 2022)** coupled with significant increase of $K_2O$ (Table 5) indicate that the ADG melts are enriched in F and total alkali, which decrease the viscosity of the magma (**Giordano *et al.*, 2004**) and hence facilitate and prolong fractional crystallization (Fig. 10e, f; **Zhu *et al.*, 2002**). These trends, together with the presence of F-rich fluids, are typical of highly evolved rare-metal granites where crystallization and fluid–melt interaction profoundly shape the residue's chemistry. Accordingly we acknowledge that, ADG was derived from magmas that resulted from the partial melting of crustal components, followed by extensive fractional crystallization.

The $Zr/TiO_2$ ratio serves as a significant indicator of compositional changes during the magmatic evolution of felsic and intermediate rocks **(Lentz, 1996 and Syme, 1998)**. Throughout fractional crystallization, Zr and Ti exhibit contrasting fractionation patterns, where increase in Zr concurrent with a decrease of $TiO_2$ **(Barrett and MacLean, 1994)**. The ADG samples exhibit a positive covariation between Zr and $TiO_2$ (Fig. 11a), whereas they plot near the crustal field (Fig. 11b), where it was suggested to attributed to attributed to crustal melting processes **(**e.g., **Lentz, 1996 and Motoki *et al.*, 2015)**, where the differing solubilities and melting behaviours of accessory minerals (i.e., zircon, rutile, and ilmenite) influence the trace element composition of the resulting melts **(Lentz, 1996)**. Consequently, we suggested that the ADG A-type granite originated from crustal sources. Accordingly, we hypothesize that the ADG was likely generated through minimal degree of partial melting of crustal materials.

**Proposed petrogenetic Model for Abu Dabbab Rare-Metal Mineralization**

**Whalen and Hildebrand (2019)** have maintained that certain elemental ratios (e.g., Sr/Y=20, Nb/Y=0.4, Ta/Yb=0.3, La/Yb=10.0, Gd/Yb=2.0, Sm/Yb=2.5, Y+Nb=60) distinguish arc, slab failure and A-type compositions. ADG data fall in the field of A-type granites (Fig. 11c), whereas they plot in the fields of post-collision and within-plate setting (Figs. 11d, e), consistent with the prevalent A-type granites elsewhere (e.g., **Haapala *et al.*, 2007; Wang *et al.*, 2020 and Xiao *et al.*, 2023)** and in the ANS, which are mainly attributed to magmatic sources in continental crust or island-arc magmatism **(Azer *et a*l., 2023; El-Awady *et al.*, 2024; Jarrar *et al.*, 2008)**. Accordingly, ABD were emplaced during the post-collisional phase of the ANS evolution, following the collision of the juvenile ANS crust with the ancient pre-Neoproterozoic continental blocks of West Gondwana Saharan Metacraton **(Liégeois *et al.*, 2013)**

Based on the previous data and conclusions taking in consideration the the previous literature about ADG ( **Sami *et al.*, 2017 ; Moussa *et al.*, 2021 ; Abdelfadil *et al.*, 2022a ; El-Desoky et al., 2022 and Azer *et al.*, 2023)** we acknowledge that, during the transitional phase from compression to extension of the ANS, the ADG experienced significant lithospheric thinning through slab breakoff and delamination—a process that led to the underplating of mantle-derived mafic magmas beneath the crust. Such tectonic unroofing is well-documented in post-collisional orogens, where it similarly drives mantle magmatism and crustal melting **(Huw Davies and von Blanckenburg, 1995 ; Tang *et al.*, 2024)**. Basaltic underplating introduced a heat pulse and volatiles ($H_2O$, F, Cl, B, HFSEs, alkalis) that migrated upward, pre-saturating the overlying crust in fluxing elements. This promoted the melting of mica-bearing crustal rocks, enriched further in fluorine as dehydrating crustal minerals broke down **(Azer *et al.*, 2019a and Azer *et al.*, 2020)**. Structural pathways such as faults and shear zones served as conduits for these volatile-rich magmas, enabling them to intrude at shallower depths (Fig. 11f).

Within these crustal melts, fluorine played a critical role: reducing magma viscosity and solidus temperature, extending crystallization time, and markedly enhancing the solubility of HFSEs like Nb, Ta, and Sn—resulting in their incompatible behavior and enrichment in the final magma **(Aseri *et al.*, 2015)**

The result was a highly differentiated, peraluminous granitic melt, enriched in Sn–Nb–Ta. This melt crystallized at shallow crustal levels to form the Abu Dabbab rare-metal granite. Residual, volatile-rich fluids migrated upward into the roof of the intrusion, leading to greisen and quartz vein mineralization enriched in Ta–Sn.

**Table 5. Geochemical composition, calculated CIPW normative minerals and pressure/depth estimates of ADG, central Eastern Desert, Egypt.**

| Rock type | Gneissose granite | | | | | | | | | | |
|---|---|---|---|---|---|---|---|---|---|---|---|
| Sample | K7 | K20 | K2 | K12 | K14 | K4 | K10 | K15 | K8 | K17 | K22 |
| $SiO_2$ | 70.89 | 72.27 | 72.44 | 73.31 | 73.46 | 73.54 | 73.97 | 74.58 | 72.89 | 75.07 | 76.62 |
| $TiO_2$ | 0.06 | 0.04 | 0.04 | 0.04 | 0.04 | 0.04 | 0.03 | 0.04 | 0.04 | 0.04 | 0.04 |
| $Al_2O_3$ | 16.20 | 15.90 | 16.22 | 15.10 | 14.72 | 13.84 | 15.79 | 14.77 | 16.04 | 15.14 | 13.44 |
| $FeO^t$ | 0.50 | 0.26 | 0.47 | 0.16 | 0.40 | 0.41 | 0.17 | 0.23 | 0.27 | 0.31 | 0.26 |
| MnO | 0.47 | 0.21 | 0.81 | 0.28 | 0.15 | 0.41 | 0.14 | 0.33 | 0.49 | 0.49 | 0.48 |
| MgO | 0.15 | 0.06 | 0.04 | 0.03 | 0.03 | 0.11 | 0.03 | 0.05 | 0.05 | 0.09 | 0.05 |
| CaO | 0.40 | 0.19 | 0.16 | 0.16 | 0.12 | 0.11 | 0.11 | 0.09 | 0.06 | 0.04 | 0.03 |
| $Na_2O$ | 4.85 | 4.45 | 5.96 | 6.10 | 6.15 | 6.17 | 6.61 | 7.17 | 5.73 | 5.10 | 6.25 |
| $K_2O$ | 4.19 | 4.63 | 3.68 | 3.10 | 2.76 | 2.75 | 2.88 | 2.45 | 3.84 | 3.22 | 2.20 |
| $P_2O_5$ | 0.07 | 0.06 | 0.07 | 0.06 | 0.06 | 0.07 | 0.07 | 0.05 | 0.07 | 0.05 | 0.05 |
| LOI | 0.59 | 0.61 | 0.52 | 0.33 | 0.47 | 0.52 | 0.37 | 0.44 | 0.55 | 0.35 | 0.51 |
| Total | 98.37 | 98.68 | 100.41 | 98.67 | 98.36 | 97.97 | 100.17 | 100.20 | 100.03 | 99.90 | 99.93 |
| Mg# | 23.08 | 18.75 | 7.84 | 15.79 | 6.98 | 21.15 | 15.00 | 17.86 | 15.63 | 22.50 | 16.13 |
| | Some of calculated CIPW normative minerals | | | | | | | | | | |
| Quartz | 32.65 | 31.21 | 31.28 | 34.21 | 34.60 | 42.48 | 33.13 | 37.38 | 34.43 | 37.75 | 43.43 |
| Corundum | 1.33 | 1.49 | 2.04 | 1.35 | 1.08 | 3.56 | 1.49 | 1.42 | 0.00 | 1.86 | 1.35 |
| Orthoclase | 13.00 | 21.92 | 16.78 | 21.75 | 14.48 | 21.45 | 20.33 | 16.25 | 24.23 | 16.31 | 12.94 |
| Albite | 61.35 | 52.72 | 56.95 | 50.43 | 56.86 | 37.65 | 54.41 | 52.21 | 49.68 | 52.04 | 49.50 |
| Anorhite | 1.53 | 0.40 | 0.09 | 0.09 | 0.02 | 0.09 | 0.09 | 0.62 | 0.09 | 0.47 | 0.27 |

**Table 5: (continued)**

| Rock type | Gneissose granite | | | | | | | | | | |
|---|---|---|---|---|---|---|---|---|---|---|---|
| **Sample** | **K7** | **K20** | **K2** | **K12** | **K14** | **K4** | **K10** | **K15** | **K8** | **K17** | **K22** |
| | **Trace and REE elements contents (ppm)** | | | | | | | | | | |
| **V** | 15.00 | <8 | <8 | <8 | <8 | <8 | 15.00 | 23.00 | <8 | 9.00 | 13.00 |
| **Ni** | 1.40 | 1.70 | 0.90 | 13.30 | 1.20 | 2.40 | 17.50 | 3.20 | 4.00 | 4.40 | 3.40 |
| **Zn** | 399.00 | 304.00 | 177.00 | 782.00 | 91.00 | 197.00 | 295.00 | 442.00 | 244.00 | 163.00 | 245.00 |
| **Cs** | 2.10 | 3.00 | 3.10 | 4.90 | 1.90 | 2.10 | 3.30 | 2.00 | 2.60 | 2.70 | 3.80 |
| **Rb** | 447.20 | 704.60 | 727.70 | 640.40 | 523.70 | 465.00 | 386.10 | 382.30 | 588.10 | 474.30 | 618.80 |
| **Sr** | 70.00 | 56.00 | 55.00 | 56.00 | 51.00 | 64.00 | 70.00 | 74.00 | 70.00 | 55.00 | 71.00 |
| **Y** | 1.00 | 0.30 | 0.50 | 0.40 | 0.60 | 0.70 | 0.80 | 0.80 | 0.40 | 0.30 | 0.40 |
| **Zr** | 55.50 | 36.30 | 34.30 | 29.50 | 46.40 | 25.10 | 95.00 | 34.90 | 34.40 | 27.50 | 66.20 |
| **Nb** | 58.00 | 68.40 | 69.90 | 39.50 | 43.60 | 70.10 | 113.10 | 20.80 | 77.40 | 32.80 | 116.60 |
| **Ba** | 22.20 | 12.70 | 4.10 | 21.30 | 18.90 | 10.70 | 58.90 | 16.50 | 9.30 | 23.70 | 10.00 |
| **Hf** | 37.40 | 17.40 | 17.60 | 13.00 | 23.90 | 12.40 | 63.30 | 17.80 | 15.30 | 13.20 | 42.90 |
| **Ta** | 106.80 | 103.80 | 117.70 | 57.60 | 102.00 | 70.10 | 425.40 | 49.10 | 111.20 | 65.30 | 544.00 |
| **Pb** | 57.70 | 22.70 | 30.50 | 23.90 | 19.70 | 25.00 | 18.10 | 27.60 | 33.90 | 20.60 | 16.90 |
| **Th** | 7.30 | 6.40 | 4.80 | 3.40 | 6.10 | 5.80 | 9.90 | 4.30 | 6.10 | 5.10 | 6.90 |
| **U** | 5.70 | 5.30 | 5.00 | 2.90 | 4.60 | 4.60 | 12.00 | 4.00 | 5.10 | 3.80 | 8.10 |
| **La** | 1.39 | 1.31 | 1.87 | 1.67 | 1.25 | 1.17 | 1.45 | 1.19 | 1.15 | 1.05 | 1.21 |
| **Ce** | 7.49 | 7.32 | 9.37 | 6.22 | 3.72 | 4.63 | 8.06 | 3.89 | 5.94 | 6.75 | 9.18 |
| **Pr** | 1.13 | 0.98 | 1.17 | 1.09 | 0.58 | 0.59 | 1.08 | 0.46 | 0.76 | 0.97 | 1.04 |
| **Nd** | 1.61 | 2.10 | 1.90 | 2.14 | 1.23 | 2.80 | 1.20 | 1.15 | 1.16 | 1.40 | 1.37 |
| **Sm** | 0.73 | 0.78 | 0.89 | 0.75 | 0.57 | 0.99 | 0.49 | 0.51 | 0.53 | 0.69 | 0.88 |
| **Eu** | 0.02 | 0.02 | 0.02 | 0.02 | 0.02 | 0.02 | 0.02 | 0.01 | 0.01 | 0.01 | 0.01 |
| **Gd** | 0.41 | 0.38 | 0.36 | 0.39 | 0.28 | 0.31 | 0.44 | 0.23 | 0.38 | 0.37 | 0.42 |
| **Tb** | 0.32 | 0.19 | 0.16 | 0.17 | 0.13 | 0.26 | 0.27 | 0.15 | 0.27 | 0.25 | 0.18 |
| **Dy** | 2.11 | 1.56 | 1.87 | 1.81 | 1.85 | 2.56 | 1.63 | 1.93 | 2.53 | 1.92 | 1.99 |
| **Ho** | 0.45 | 0.29 | 0.24 | 0.31 | 0.27 | 0.49 | 0.39 | 0.29 | 0.53 | 0.38 | 0.40 |
| **Er** | 1.39 | 1.91 | 2.03 | 1.74 | 1.31 | 2.14 | 1.83 | 1.25 | 2.49 | 1.82 | 1.59 |
| **Tm** | 0.63 | 0.49 | 0.47 | 0.45 | 0.98 | 0.91 | 0.54 | 0.94 | 0.93 | 0.75 | 0.69 |
| **Yb** | 9.13 | 7.68 | 7.43 | 6.24 | 11.25 | 10.16 | 8.64 | 10.89 | 7.34 | 8.96 | 7.36 |
| **Lu** | 0.83 | 0.91 | 0.88 | 1.03 | 1.84 | 1.89 | 0.86 | 1.72 | 1.69 | 1.51 | 0.89 |
| **∑REE** | 27.64 | 25.92 | 28.66 | 24.03 | 25.28 | 28.92 | 26.90 | 24.61 | 25.71 | 26.83 | 27.21 |

**Table 5: (continued)**

| Rock type | Alkali feldspar granites | | | | | | | | | | |
|---|---|---|---|---|---|---|---|---|---|---|---|
| **Sample** | **K7** | **K20** | **K2** | **K12** | **K14** | **K4** | **K10** | **K15** | **K8** | **K17** | **K22** |
| **Q`** | **30.08** | **29.37** | **29.76** | **32.13** | **32.66** | **41.78** | **30.69** | **35.12** | **31.75** | **35.43** | **40.92** |
| **ANQR** | **10.51** | **1.80** | **0.53** | **0.41** | **0.13** | **0.41** | **0.44** | **3.65** | **0.37** | **2.79** | **2.04** |
| **$CaO/Na_2O$** | **0.08** | **0.04** | **0.03** | **0.03** | **0.02** | **0.02** | **0.02** | **0.01** | **0.01** | **0.01** | **0.00** |
| **A/CNK** | **1.22** | **1.25** | **1.15** | **1.10** | **1.10** | **1.04** | **1.11** | **1.01** | **1.17** | **1.27** | **1.06** |
| **A/NK** | **1.29** | **1.29** | **1.18** | **1.13** | **1.12** | **1.05** | **1.13** | **1.02** | **1.18** | **1.27** | **1.06** |
| **AI** | **0.88** | **0.90** | **0.87** | **0.91** | **0.93** | **0.76** | **0.91** | **0.89** | **1.00** | **0.87** | **0.89** |
| **K/Rb** | **77.78** | **54.55** | **41.98** | **40.19** | **43.75** | **49.10** | **63.06** | **39.67** | **61.93** | **53.20** | **40.09** |
| **Nb/Ta** | **0.54** | **0.66** | **0.59** | **0.69** | **0.43** | **1.00** | **0.27** | **0.45** | **0.27** | **0.42** | **0.70** |
| **Zr/Hf** | **1.59** | **0.93** | **0.80** | **0.63** | **2.21** | **1.09** | **3.11** | **1.22** | **2.64** | **1.66** | **1.27** |
| **Rb/Ba** | **20.14** | **55.48** | **177.49** | **30.07** | **27.71** | **43.46** | **135.67** | **93.51** | **6.56** | **23.17** | **63.24** |
| **La/Sm** | **1.90** | **1.68** | **2.10** | **2.23** | **2.19** | **1.18** | **2.16** | **1.84** | **2.96** | **2.33** | **2.17** |
| **Rb/Sr** | **6.39** | **12.58** | **13.23** | **11.44** | **10.27** | **7.27** | **7.51** | **18.00** | **5.52** | **5.17** | **8.40** |
| **Hf/Ta** | **0.33** | **0.38** | **0.37** | **0.82** | **0.21** | **0.33** | **0.19** | **0.29** | **0.08** | **0.43** | **0.24** |
| **Th/Ta** | **0.07** | **0.06** | **0.04** | **0.06** | **0.06** | **0.08** | **0.03** | **0.03** | **0.02** | **0.09** | **0.05** |
| **Nb/U** | **10.18** | **12.91** | **13.98** | **13.62** | **9.48** | **15.24** | **4.91** | **12.76** | **9.43** | **5.20** | **15.18** |
| **Th/U** | **1.28** | **1.21** | **0.96** | **1.17** | **1.33** | **1.26** | **0.57** | **0.73** | **0.83** | **1.08** | **1.20** |
| **Eu/Eu*** | **0.10** | **0.10** | **0.09** | **0.10** | **0.14** | **0.09** | **0.12** | **0.10** | **0.13** | **0.08** | **0.06** |
| ***T(°C)** | **759.07** | **814.67** | **720.81** | **854.72** | **708.43** | **663.45** | **799.56** | **794.42** | **714.87** | **764.72** | **777.55** |
| **Pressure (kbar) and depth (Km) estimation using normative minerals (Qtz and Or+Ab) based on polynomial equations of Yang (2017)** | | | | | | | | | | | |
| **$P_{Qtz}$** | **2.06** | **1.94** | **1.74** | **2.09** | **1.63** | **1.54** | **1.58** | **1.34** | **1.09** | **1.72** | **1.66** |
| **Depth** | **5.07** | **5.04** | **4.70** | **4.26** | **4.40** | **4.15** | **4.26** | **3.63** | **4.94** | **4.65** | **4.48** |
| **$P_{(Or+Ab)}$** | **2.78** | **1.73** | **4.20** | **3.01** | **1.44** | **5.23** | **3.60** | **1.18** | **2.13** | **3.16** | **1.28** |
| **Depth** | **4.49** | **4.68** | **4.34** | **4.12** | **3.89** | **4.11** | **4.72** | **3.19** | **4.76** | **4.52** | **3.45** |

FeO* refers to total Fe is expressed as FeO; (AI = (Na+K)/Al (atom %) is the calculated agpaitic index; n.d. = not determined; Ce* = $CeN/(La_N^{2/3}xNd_N^{1/3})$; $Tb^*=Tb_N/(Gd_N^{2/3}xHo_N^{1/3})$; $Dy^*=Dy_N/(Gd_N^{1/3}xHo_N^{2/3})$; $TE_3=(Tb^*xDy^*)^{1/2}$.

*T(°C) values were calculated based on the method $T_{(°C)} = -15{,}993/ (\ln C_{Zr} + \ln C_{Hf} - 21.668 - 273)$ of **Daneshvar *et al.* (2022),** where $C_{Zr}$ and $C_{Hf}$ are the bulk-rock Zr and Hf contents in ppm.

$P_{Qtz} = -0.2426 \times (Qtz)3 + 26.392 \times (Qtz)2 \times -980{:}74 \times (Qtz) + 12563$

$P_{(Or+Ab)} = 0.2426 \times (Ab+Or)3 - 46.397 \times (Ab+Or)2 \times -2981.3 \times (Ab+Or) - 64224$

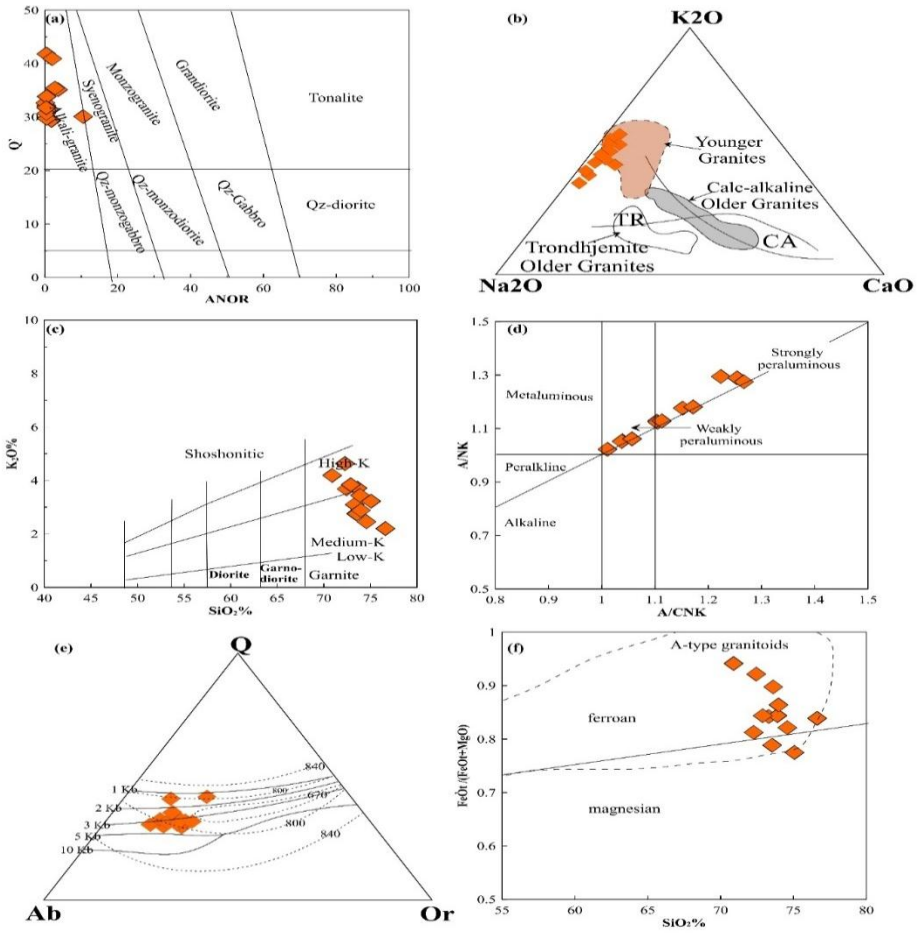


**Fig. 7.** Geochemical characteristics of ADG (a) Q` [100*Q/(Q+Or+Ab+An)] vs. ANOR [100×An/(Or+An)] diagram for normative classification of the studied granite (Streckeisen & Le Maitre, 1979); (b) Classification diagram of the Egyptian granitic rocks after **(Hassan & Hashad, 1990)**. The trondhjemite (TR) and calc-alkaline (CA) trends are from (Barker & Arth, 1976); (c) Plot of the SKGG samples on the mol. $Al_2O_3/(Na_2O+K_2O)$ (A/NK) vs. alumina saturation index (A/CNK) [$A/CNK=Al_2O_3/(CaO+Na_2O+K_2O)$] diagram of **Zen (1986)**; d) $K_2O$ vs. $SiO_2$ variation diagram for the studied granitic rocks. Field are after **(Rickwood, 1989)**; (e) $SiO_2$ versus FeOt/(FeOt +MgO) variation diagram for ADG plots fields are after **(Frost *et al.*, 2001);** (f) Normative composition of the AKAG plotted in the haplogranite system Q-Ab-Or-$H_2O$ (**Tuttle and Bowen, 1958**). The dotted line shows the locations of minima melt compositions at saturated water pressures ranging from 0.5 kbar to 10 kbar **(Johannes, 1980)**. (g) $SiO_2$ versus FeOt/(FeOt +MgO) variation diagram for SKGG plots fields are after **(Frost *et al.*, 2001)**.

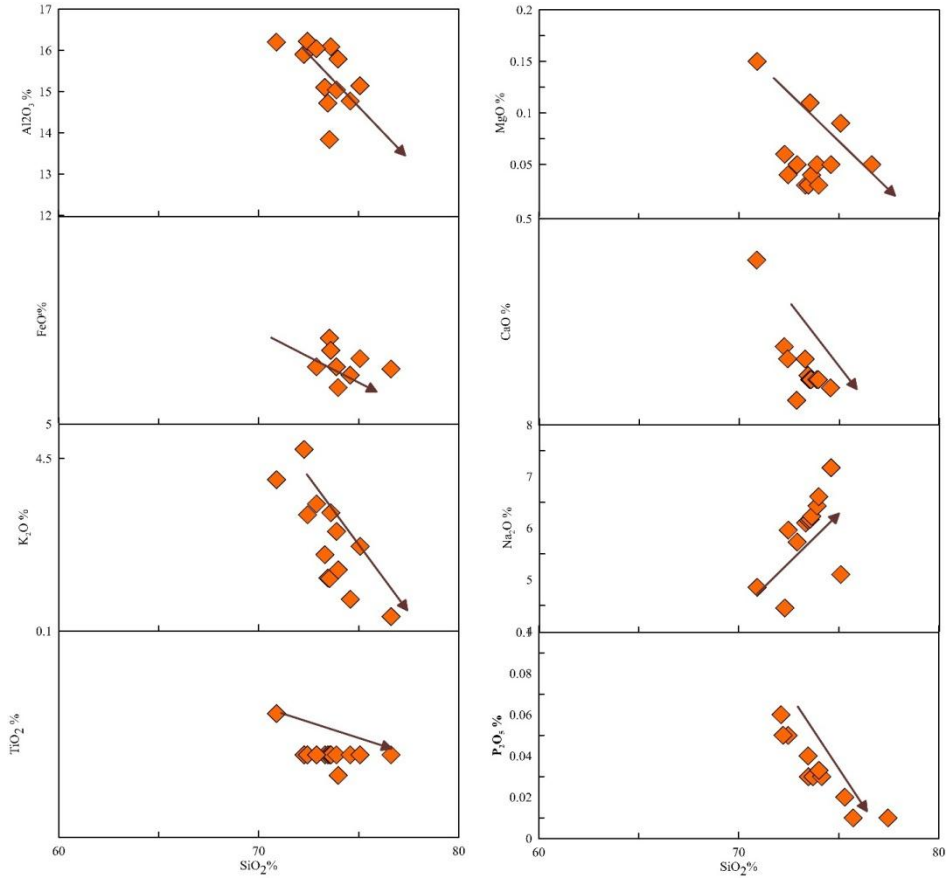


**Fig. 8:** Harker variation diagrams for the major oxides of the studied granite.

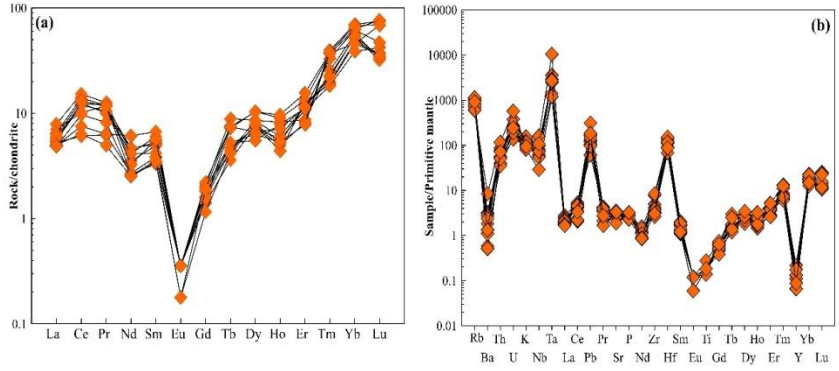


Fig.9. Trace elements abundances. (a) Chondrite-normalized REE patterns for the studied granitic rocks; and (b) Primitive mantle-normalized multi-element patterns of trace elements in the studied granitic rocks. Primitive mantle concentrations from (S.-S. Sun & McDonough, 1989).

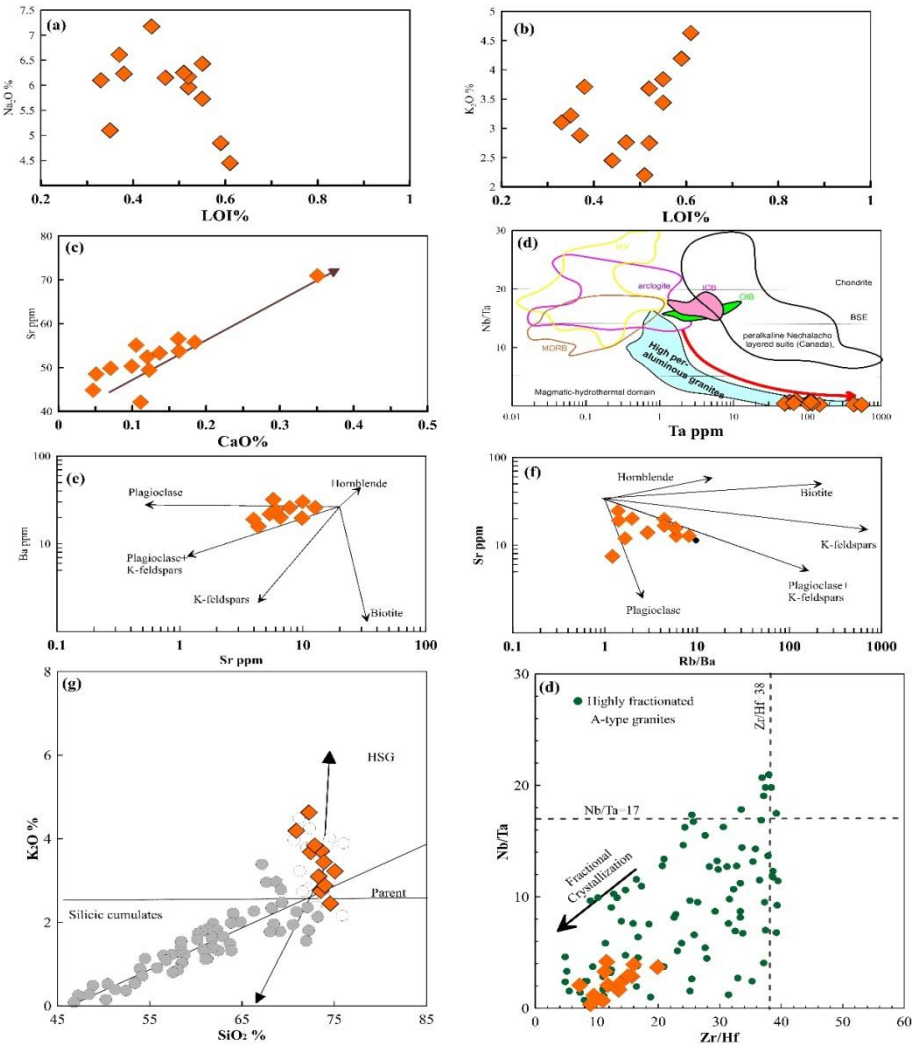


**Fig. 10.** (a, b) variation diagrams of LOI vs, whole rock contents of (a) $Na_2O$ and (b) $K_2O$. (c) variation diagram of between whole rock CaO wt.% and Sr (ppm). (d) Variation of whole rock Ta (ppm) and Nb/Ta ratio of ADG Field and limitations after **(Ballouard *et al.*, 2016).** (e, f) Variation diagrams of whole rock contents of (e) Sr and Br and (f) Sr vs. Rb/Ba, Rayleigh fractionation vectors from **(Keskin, 2002; Tindleand Pearce, 1981).** (g) Covariations of $K_2O$ vs. $SiO_2$ contents. In this diagram, data points of the present study plot along a trend defined by the Peninsular Ranges Batholith in California (high silica granite, grey and open circle). Data of High Silica Granites are from **Lee and Morton (2015).** (h) Plots of ADG samples on Zr/Hf-Nb/Ta variation diagram. Fields and data of highly fractionated A-type granite after **Wu *et al.* (2017)**.

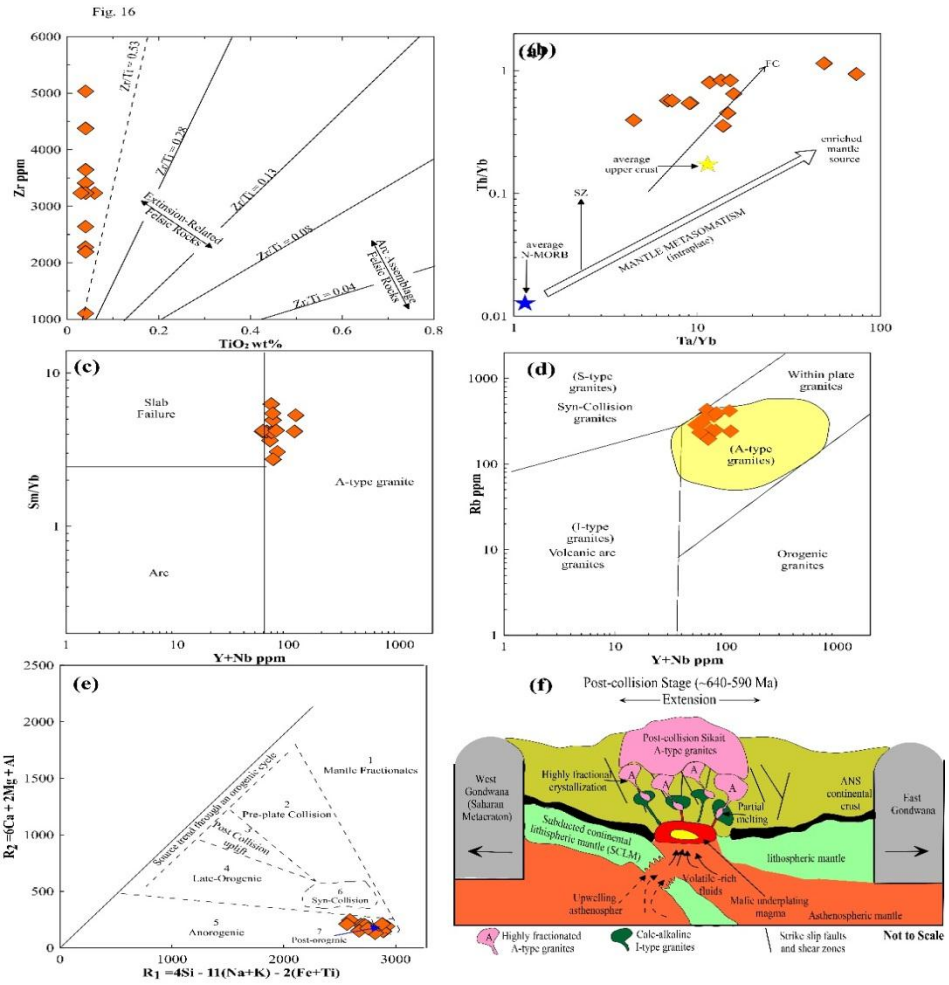


**Fig. 11.** (a) Zr vs. $TiO_2$ **(Syme, 1998)** for ADG samples. Double-sided arrows indicate ranging of different fields: Arc rhyolites assemblages (tholeiitic and calc-alkaline arc suites) have $Zr/TiO_2$ ratios ranging from about 0.016 to 0.04, and extension-related rhyolites from about 0.13 to 0.28 **(Syme, 1998)**. (b) Th/Yb vs. Ta/Yb diagram for the studied ADG after **(Jahn, *et al.*, 1999)**. (c) Y+Nb vs. Sm/Yb ratio discrimination plots are used to separate arc, slab failure compositions. Coordinates for plot fields are based on these values: Sm/Yb (2.5) and Nb + Y (60) **(Whalen and Hildebrand, 2019);** (d) Rb vs. Y+Nb tectonic discrimination diagram **(Christiansen and Keith, 1996; Pearce, 1996)**. (e) R1-R2 diagram (Batchelor & Bowden, 1985) showing the major tectonic associations of SKGG. R1=4 Si-11(Na+K)-2(Fe+Ti); R2=6Ca+2Mg+Al. (f) Simplified model for the tectonomagmatic evolution of the juvenile crust in the ADG in the Eastern Desert of Egypt, demonstrating A-type granite formation during the post-collisional stage. This stage shows lithospheric, partial melting of lower crust and the generation of A-type granites in the upper crust modified after **(Sami *et al.*, 2018).**

## CONCLUSION

1. The Abu Dabbab Neoproterozoic granites represent the most significant Sn–Ta–Zr-rich intrusions within Egypt's Central Eastern Desert, composed predominantly of albite, K- feldspar, and Li-phengite, with accessory minerals like columbite–tantalite, cassiterite, and hafnium-rich zircon.
2. These granites were emplaced shallowly during the ANS's transitional tectonic stage (~650–690 Ma), under a highly fractionated calc-alkaline, peraluminous, intraplate setting .
3. Its geochemical signatures include: High Rb/Sr ratios, Elevated Ta, Nb, and strong and aligning it with muscovite-bearing, peraluminous rare-metal granites
4. The magma originated via melting of juvenile crust, triggered by asthenospheric underplating, with the injected volatiles enriching the melt with F and other ions. Subsequent mica decomposition increased fluorine, promoting intensive fractional crystallization of feldspars and other minerals.
5. Fluorine decreased the melt viscosity and increased the solubility of HFSEs (Nb, Ta, Sn) by forming fluorine complexes,
6. Cooler residual melts crystallized economically important Ta–Nb–Sn bearing minerals,
7. Late-stage exsolved fluids contributed to greisen and quartz vein mineralization enriched in Sn–Ta.

## REFERENCES

**Abdel-Rahman, A. (2006):** Petrogenesis of anorogenic peralkaline granitic complexes from eastern Egypt. Mineralogical Magazine, 70(1): 27-50.

**Abdelfadil, K. ; P. Asimow ; M. Azer and H. Gahlan (2016):** Genesis and petrology of Late Neoproterozoic pegmatites and aplites associated with the Taba metamorphic complex in southern Sinai, Egypt. Geológica Acta, 14(3): 219-235.

**Abdelfadil, K.M. ; M.E. Gharib ; P. Uher and M. Putiš (2022):** Petrogenesis of post-orogenic Pan-African rare-element granitic pegmatites in the western Arabian-Nubian Shield, Aswan area, southern Egypt. J. Asian Earth Sci., 224: 105003. -

**Abdelfadil, K.M. ; N.M. Mahdy ; M. Ondrejka and M. Putiš (2022):** Mineral chemistry and monazite chemical Th-U-total Pb dating of the Wadi Muweilha muscovite pegmatite, Central Eastern Desert of Egypt: constraints on its origin and geodynamic evolution relative to the Arabian Nubian Shield. Int. J. Earth Sci., 111: 823–860.

**Abdelfadil, K.M. ; G.M. Saleh ; M. Putiš and M. Sami (2022):** Mantle source characteristics of the late Neoproterozoic post-collisional gabbroic intrusion of Wadi Abu Hadieda, north Arabian-Nubian Shield, Egypt. J. African Earth Sci., 194: 104607.

**Abuamarah, B.A. ; M.K. Azer ; A.M. Seddik ; P.D. Asimow ; P. Guzman ; B.T. Fultz and M.H. Darwish (2021):** Magmatic and post-magmatic evolution of post-collisional rare-metal bearing granite: The neoproterozoic homrit akarem granitic intrusion, south eastern desert of egypt, arabian-nubian shield. Geochemistry (Chemie der Erde), 82: 128540.

**Aseri, A.A. ; R.L. Linnen ; X.D. Che ; Y. Thibault and F. Holtz (2015):** Effects of fluorine on the solubilities of Nb, Ta, Zr and Hf minerals in highly fluxed water-saturated haplogranitic melts. Ore Geol. Rev., 64: 736-746.

**Azer, M.K. (2013):** Late Ediacaran (605–580 Ma) post-collisional alkaline magmatism in the Arabian–Nubian Shield: A case study of Serbal ring-shaped intrusion, southern Sinai, Egypt. J. Asian Earth Sci., 77: 203-223.

**Azer, M. ; K. Abdelfadil and A. Ramadan (2019):** The Nuweibi rare-metal albite granite: A magmatic cupola above a highly fractionated post-collisional A-type granite pluton. J. Geol., 10, x.

**Azer, M.K. ; K.M. Abdelfadil and A.A.Ramadan (2019):** Geochemistry and petrogenesis of Late Ediacaran Rare-Metal Albite Granite of the Nubian Shield: Case study of Nuweibi Intrusion, Eastern Desert, Egypt. J. Geol., 127(6): 665-689.

**Azer, M.K. ; K.M. Abdelfadil ; P.D. Asimow and A.E. Khalil (2020):** Tracking the transition from subduction-related to post-collisional magmatism in the north Arabian–Nubian Shield: A case study from the Homrit Waggat area of the Eastern Desert of Egypt. Geological J., 55(6): 4426-4452.

**Azer, M.K. ; B.A. Abuamarah ; M.M. Srour ; S.A. Wilde and R.M. Gomaa (2023):** Mineralogy, geochemistry, and petrogenesis of postcollisional granites from the arabian-nubian shield: Case study from the gabal nugrus area in the south eastern desert of Egypt. J. Geol., 131(3): 221-263.

**Ballouard, C. ; M. Poujol ; P. Boulvais ; Y. Branquet ; R. Tartèse and J.L. Vigneresse (2016):** Nb-Ta fractionation in peraluminous granites: A marker of the magmatic-hydrothermal transition. Geol., 44(3): 231-234.

**Barker, F. and J.G. Arth (1976):** Generation of trondhjemitic-tonalitic liquids and Archean bimodal trondhjemite-basalt suites. Geology, 4(10): 596-600.

**Barrett, T.J. and W.H.MacLean, (1994):** Chemostratigraphy and hydrothermal alteration in exploration for VHMS deposits in greenstones and younger volcanic rocks. Alteration and alteration processes associated with ore-forming systems: Geological Association of Canada, Short Course Notes, 11: 433-467.

**Batchelor, R.A. and P. Bowden (1985):** Petrogenetic interpretation of granitoid rock series using multicationic parameters. Chem. Geol., 48(1-4): 43-55.

**Bonin, B. (2007):** A-type granites and related rocks: evolution of a concept, problems and prospects. Lithos, 97(1): 1-29.

**Breiter, K. ; J. Kynický and Z. Korbelová (2024).** Chemical and textural peculiarities of zircon from peralkaline granites and quartz-bearing syenites. Minerals, 14(2). doi:10.3390/min14020187

**Castorina, F. ; U. Masi ; G. Padalino and M. Palomba (2006):** Constraints from geochemistry and Sr-Nd isotopes for the origin of albitite deposits from Central Sardinia (Italy). Mineralium Deposita, 41(4): 323-338.

**Champion, D.C. and B.W. Chappell (1992):** Petrogenesis of felsic I-type granites: an example from northern Queensland. Earth Environmental Science Transactions of the Royal Society of Edinburgh, 83(1-2): 115-126.

**Christiansen, E.H. and J.D. Keith (1996):** Trace-element systematics in silicic magmas: A metallogenic perspective. In: Wyman, D.A. (Ed.), Trace Element Geochemistry of Volcanic Rocks: Applications for Massive Sulphide Exploration. Geological Association of Canada, Short Course Notes, 12: 115-151.

**Collins, W. ; S.Beams ; A. White and B. Chappell (1982):** Nature and origin of A-type granites with particular reference to southeastern Australia. Contributions to Mineral. and Petrol., 80(2): 189-200.

**Creaser, R.A. ; R.C. Price and R.J. Wormald (1991):** A-type granites revisited: assessment of a residual-source model. Geology, 19(2): 163-166.

**Deer, W. ; R. Howie and J. Zussman (1992)**: An Introduction To The Rock-Forming Minerals (2nd ed.): Harlow, Essex, England : New York, NY : Longman Scientific & Technical

**El-Awady, A. ; M. Sami ; R. Abart ; D. Fathy ; E.S. Farahat ; M.S. Ahmed and A. Ragab (2024).** Petrogenesis and Tectonic Evolution of I- and A-Type Granites of Mount Abu Kibash and Tulayah, Egypt: Evidence for Transition from Subduction to Post-Collision Magmatism. Minerals, 14(8). doi:10.3390/min14080806

**El-Desoky, H.M. ; A.M. Abdel-Rahman ; A. Ene ; A.E. Khalil, W. Fahmy ; H.M.H. Zakaly and H.A. Awad (2022).** Origin and Heavy Metals of Plagio-Granites in Egyptian Shield Oceanic Complexes: A Case Study of Abu Dabbab Area, Central Eastern Desert, Egypt. Minerals, 12(9). doi:10.3390/min12091093

**El Hadek, H.H. ; M.A. Mohamed ; G.H. El-Habaak ; W.W. Bishara and K.A. Ali (2016):** Geochemical constraints on petrogenesis of

Homrit Waggat rare metal granite, Egypt. Int. J. Geophysics and Geochem., 3(4), 33-48.

**Eliwa, H.A. ; C. Breitkreuz ; M. Murata ; I.M. Khalaf ; B. Bühler ; T. Itaya and T. Shibata (2014):** SIMS zircon U–Pb and mica K–Ar geochronology, and Sr–Nd isotope geochemistry of Neoproterozoic granitoids and their bearing on the evolution of the north Eastern Desert, Egypt. . Gondwana Res., 25(4): 1570-1598.

**Feteha, B.F.E. ; D.R. Lentz ; A.M. El-Bouseily ; K.I. Khalil ; H.A. Khamis and A.K.M. Moghazi (2022):** Petrogenesis of neoproterozoic Mo-bearing A-type granites in the Gattar area, northern Eastern Desert, Egypt: Implications for magmatic evolution and mineralization processes. Ore Geol. Rev., 148: doi:10.1016/j.oregeorev.2022.105007

**Frost, B.R. ; C.G. Barnes ; W.J. Collins ; R.J. Arculus ; D.J. Ellis and C.D. Frost (2001):** A geochemical classification for granitic rocks. J. Petrol., 42(11): 2033-2048.

**Giordano, D. ; C. Romano ; D.B. Dingwell ; B. Poe and H. Behrens (2004):** The combined effects of water and fluorine on the viscosity of silicic magmas. Geochimica et Cosmochimica Acta, 68(24): 5159-5168.

**Haapala, I. ; S. Frindt and J. Kandara (2007):** Cretaceous Gross Spitzkoppe and Klein Spitzkoppe stocks in Namibia: Topaz-bearing A-type granites related to continental rifting and mantle plume. Lithos, 97(1-2), 174-192.

**Hanson, G. N. (1978):** The application of trace elements to the petrogenesis of igneous rocks of granitic composition. Earth and Planetary Sci. Letters, 38(1): 26-43.

**Hassan, M.A. and A.H. Hashad (1990):** Precambrian of Egypt. In: Said, R. (Ed.), The Geology of Egypt. Balkema, Rotterdam, Pp: 201–245.

**He, J. ; X. Xu ; Z. Fu ; Y. An ; T. Chen ; Q. Xie and F. Chen (2021).** Decoupling of Sr-Nd Isotopic Composition Induced by Potassic Alteration in the Shapinggou Porphyry Mo Deposit of the Qinling–Dabie Orogenic Belt, China. Minerals, 11(8). doi:10.3390/min11080910

**Heikal, M.T.S. ; M.Z. Khedr ; M. Abd El Monsef and S.R. Gomaa (2019):** Petrogenesis and geodynamic evolution of Neoproterozoic Abu Dabbab Albite Granite, Central Eastern Desert of Egypt: Petrological and geochemical constraints. J. African Earth Sci., 158. doi:10.1016/j.jafrearsci.2019.103518

**Huw Davies, J. and F. von Blanckenburg (1995):** Slab breakoff: A model of lithosphere detachment and its test in the magmatism and deformation of collisional orogens. Earth and Planetary Sci. Letters, 129(1): 85-102.

**Jahn, B.M. ; F. Wu ; R. Capdevila ; F. Martineau ; Z. Zhao and Y. Wang (2001):** Highly evolved juvenile granites with tetrad REE patterns: the Woduhe and Baerzhe granites from the Great Xing'an Mountains in NE China. Lithos, 59(4): 171-198.

**Jahn, B.M. ; F. Wu ; C.H. Lo and C.H.Tsai (1999):** Crust–mantle interaction induced by deep subduction of the continental crust: geochemical and Sr–Nd isotopic evidence from post-collisional mafic–ultramafic intrusions of the northern Dabie complex, central China. Chemical Geol., 157(1-2): 119-146.

**Jarrar, G.H. ; W. Manton ; R. Stern and D. Zachmann (2008):** Late Neoproterozoic A-type granites in the northernmost Arabian-Nubian Shield formed by fractionation of basaltic melts. Chemie der Erde-Geochemistry, 68(3): 295-312.

**Johannes, W. (1980):** Metastable melting in the granite system Qz-Or-Ab-An-$H_2O$. Contributions to Mineral. and Petrol., 72(1): 73-80.

**Johnson, P.R. and B. Woldehaimanot (2003):** Development of the Arabian-Nubian Shield: perspectives on accretion and deformation in the northern East African Orogen and the assembly of Gondwana. Geological Society, London, Special Publications, 206(1): 289-325.

**Keskin, M. (2002):** FC-modeler: A Microsoft® Excel© spreadsheet program for modeling Rayleigh fractionation vectors in closed magmatic systems. Computers & Geosciences, 28(8), 919-928.

**King, P. ; A. White ; B. Chappell and C. Allen (1997):** Characterization and origin of aluminous A-type granites from the Lachlan Fold Belt, southeastern Australia. J.Petrol., 38(3), 371-391.

**Lashin, A. ; M.A. Anbar ; E. Aboud ; F. Zaidi ; A. Al-Bassam ; N. Al Arifi and E. Al-Homadhi (2023).** Geochemistry and Petrogenesis of the Ediacaran Post-Collisional Granitoid Rocks in the Midyan Terrain, Northern Arabian Shield, Saudi Arabia. Minerals, 13(3): doi:10.3390/min13030379

**Lee, C.T.A. and D.M. Morton (2015):** High silica granites: Terminal porosity and crystal settling in shallow magma chambers. Earth and Planetary Sci. Letters, 409: 23-31.

**Lee, S.G. ; Y. Asahara ; T. Tanaka ; S.R. Lee and T. Lee (2013):** Geochemical significance of the Rb–Sr, La–Ce and Sm–Nd isotope systems in A-type rocks with REE tetrad patterns and negative Eu and Ce anomalies: The Cretaceous Muamsa and Weolaksan granites, South Korea. Geochem., 73(1): 75-88.

**Lentz, D.R. (1996):** Trace Element Systematics Of Felsic Volcanic Rocks Associated With Massive-Sulphide Deposits In The Bathurst Mining Camp: Petrogenetic, Tectonic And Chemostratigraphic Implications For VMS Exploration; in Wyman, D.A., ed., Trace

Element Geochemistry of Volcanic Rocks: Applications For Massive Sulphide Exploration. Geological Association of Canada, 12: 359-402.

**Li, X.H. ; Z.X. Li ; W.X. Li ; Y. Liu ; C. Yuan ; G. Wei and C. Qi (2007):** U–Pb zircon, geochemical and Sr–Nd–Hf isotopic constraints on age and origin of Jurassic I-and A-type granites from central Guangdong, SE China: a major igneous event in response to foundering of a subducted flat-slab? Lithos, 96(1-2): 186-204.

**Liégeois, J.P. ; M.G. Abdelsalam ; N. Ennih and A. Ouabadi (2013):** Metacraton: Nature, genesis and behavior. Gondwana Res., 23(1): 220-237.

**Liegeois, J.P. ; J. Navez ; J. Hertogen and R. Black (1998):** Contrasting origin of post-collisional high-K calc-alkaline and shoshonitic versus alkaline and peralkaline granitoids. The use of sliding normalization. Lithos, 45(1-4): 1-28.

**Macdonald, R. ; G. Davies ; C. Bliss ; P. Leat ; D. Bailey and R. Smith (1987):** Geochemistry of high-silica peralkaline rhyolites, Naivasha, Kenya Rift Valley. J. Petrol., 28(6): 979-1008.

**Mahdy, N.M. ; T. Ntaflos ; V. Pease ; M. Sami ; M. Slobodník ; A.A.A. Steet and D. Fathy (2020):** Combined zircon U-Pb dating and chemical Th–U–total Pb chronology of monazite and thorite, Abu Diab A-type granite, Central Eastern Desert of Egypt: Constraints on the timing and magmatic-hydrothermal evolution of rare metal granitic magmatism in the Arabian Nubian Shield. Geochem., 125669.

**Mogahed, M.M. and K.M. Abdelfadil (2021):** Constraints of Mantle And Crustal Sources Interaction During Orogenesis Of Pre-And Post-Collision Granitoids From The Northern Arabian-Nubian Shield: A Case Study From Wadi El-Akhder Granitoids, Southern Sinai, Egypt. Acta Geologica Sinica- English Edition, 95(5), 1527-1550.

**Möller, P. and G. Muecke (1984):** Significance of Europium anomalies in silicate melts and crystal-melt equilibria: A re-evaluation. Contributions to Mineral. and Petrol., 87(3): 242-250.

**Monier, G. ; J. Mergoil-Daniel and H. Labernadière (1984):** Générations successives de muscovites et feldspaths potassiques dans les leucogranites du massif de Millevaches (Massif Central français). Bulletin de Mineralogie, 107(1): 55-68.

**Motoki, A. ; S.E. Sichel ; T. Vargas ; D.P. Melo and K.F. Motoki (2015):** Geochemical behaviour of trace elements during fractional crystallization and crustal assimilation of the felsic alkaline magmas of the state of Rio de Janeiro, Brazil. Anais da Academia Brasileira de Ciências, 87.

**Moussa, H.E. ; P.D. Asimow ; M.K. Azer ; M.A. Abou El Maaty ; A.I. Akarish ; N.N. Yanni and M.A. Elsagheer (2021):** Magmatic and hydrothermal evolution of highly-fractionated rare-metal granites at Gabal Nuweibi, Eastern Desert, Egypt. Lithos, 400: 106405.

**Nesbitt, H. and G. Young (1982):** Early Proterozoic climates and plate motions inferred from major element chemistry of lutites. Nature, 299(5885), 715-717.

**Pearce, J. (1996):** Sources and settings of granitic rocks. Episodes, 19: 120-125.

**Platt, R.G. and A.R. Woolley (1986):** The mafic mineralogy of the peralkaline syenites and granites of the Mulanje complex, Malawi. Mineralogical Magazine, 50(355): 85-99.

**Rickwood, P.C. (1989):** Boundary lines within petrologic diagrams which use oxides of major and minor elements. Lithos, 22(4): 247-263.

**Sami, M. ; M.A. El-Monsef ; R. Abart ; F. Toksoy-Köksal and K.M. Abdelfadil (2022):** Unraveling the Genesis of Highly Fractionated Rare-Metal Granites in the Nubian Shield via the Rare-Earth Elements Tetrad Effect, Sr–Nd Isotope Systematics, and Mineral Chemistry. Earth Space Chem., 6(10): 2368-2384.

**Sami, M. ; T. Ntaflos ; E.S. Farahat ; H.A. Mohamed ; A.F. Ahmed and C. Hauzenberger (2017):** Mineralogical, geochemical and Sr-Nd isotopes characteristics of fluorite-bearing granites in the Northern Arabian-Nubian Shield, Egypt: Constraints on petrogenesis and evolution of their associated rare metal mineralization. Ore Geol. Rev., 88: 1-22.

**Sami, M. ; T. Ntaflos ; E.S. Farahat ; Mohamed ; H.A. ; C. Hauzenberger and A.Ahmed (2018):** Petrogenesis and geodynamic implications of Ediacaran highly fractionated A-type granitoids in the north Arabian-Nubian Shield (Egypt): constraints from whole-rock geochemistry and Sr-Nd isotopes. Lithos, 304: 329-346.

**Stern, R.J. (1994):** Arc assembly and continental collision in the Neoproterozoic East African Orogen: implications for the consolidation of Gondwanaland. Ann. Rev. of Earth and Planetary Sci., 22(1): 319-351.

**Streckeisen, A. and R.Le Maitre (1979):** A chemical approximation to the modal QAPF classification of the igneous rocks. Neues Jahrbuch für Mineralogie, Abhandlungen, 136: 169-206.

**Sun, S.S. and W. McDonough (1989):** Chemical and isotopic systematics of oceanic basalts: Implications for mantle composition and processes. Geological Society, London, Special Publications, 42(1): 313-345.

**Sun, T. ; P.Chen ; X. Zhou ; R. Wang and Z. Wang (2002):** Strongly peraluminous granites in eastern Nanling mountains, China: study on muscovites. Geological Rev., 48(5): 518-525.

**Syme, E. (1998):** Ore-associated and barren rhyolites in the central Flin Flon Belt: Case study of the Flin Flon Mine sequence. Manitoba Energy and Mines, , Open File Report OF 98-9, 1-32.

**Tang, G.J. ; D.A. Wyman ; W. Dan ; Q. Wang ; X.J. Liu ; Y.N. Yang and I. Oimahmadov (2024):** Protracted and Progressive Crustal Melting during Continental Collision in the Pamir and Plateau Growth. J. Petrol., 65(4): egae024.

**Tindle, A.G. and J.A. Pearce (1981):** Petrogenetic modelling of in situ fractional crystallization in the zoned Loch Doon pluton, Scotland. Contributions to Mineral. and Petrol., 78(2), 196-207.

**Tischendorf, G. ; B. Gottesmann ; H.J. Förster and R.B. Trumbull (1997):** On Li-bearing micas: estimating Li from electron microprobe analyses and an improved diagram for graphical representation. Mineralogical Magazine, 61(409): 809-834.

**Tuttle, O.F. and N.L. Bowen (1958)**: Origin of granite in the light of experimental studies in the system $NaAlSi_3O_8$-$KAlSi_3O_8$-$SiO_2$-$H_2O$ (Vol. 74): Geological Society of America.

**Wang, N. ; Z. Liu and M. Lei (2023).** Strongly Peraluminous Highly Fractionated I-Type Granite from Bangong–Nujiang Metallogenic Belt, Tibet: Implications for Continental Evolution and Evaluation of Economic Potentiality. Minerals, 13(9): doi:10.3390/min13091152

**Wang, X.Y. ; J.F. Qin ; S.C. Lai ; X.P. Long ; Y.J.Ju ; Z.Z. Zhang and R.Z. Zhu (2020):** Paleoproterozoic A-type granite from the southwestern margin of the North China block: high temperature melting of tonalitic crust in extensional setting. Int. Geol. Rev., 62(5): 614-629.

**Wang, X. ; W.L. Griffin and J. Chen (2010):** Hf contents and Zr/Hf ratios in granitic zircons. Geochemical J., 44(1), 65-72.

**Whalen, J.B. and R.S. Hildebrand, (2019):** Trace element discrimination of arc, slab failure, and A-type granitic rocks. Lithos, 348, 105179.

**Wu, F.Y. ; B.M. Jahn ; S.A. Wilde ; C.H. Lo ; T.F. Yui ; Q. Lin and D.Y. Sun (2003):** Highly fractionated I-type granites in NE China (II): isotopic geochemistry and implications for crustal growth in the Phanerozoic. Lithos, 67(3-4): 191-204.

**Wu, F. ; X.Liu ; W. Ji ; J. Wang and L. Yang (2017):** Highly fractionated granites: Recognition and research. Sci. China Earth Sci., 60: 1201-1219.

**Xiao, W. ; C. Liu ; K. Tan ; X. Duan ; K. Shi ; Q. Sui and F. Zi (2023).** Two Distinct Fractional Crystallization Mechanisms of A-Type

Granites in the Nanling Range, South China: A Case Study of the Jiuyishan Complex Massif and Xianghualing Intrusive Stocks. Minerals, 13(5). doi:10.3390/min13050605

**Zaraisky, G.P. ; A.M. Aksyuk ; V.N. Devyatova ; O.V. Udoratina and V.Y. Chevychelov (2009):** The Zr/Hf ratio as a fractionation indicator of rare-metal granites. Petrol., 17(1): 25-45.

**Zen, E.A. (1986):** Aluminum enrichment in silicate melts by fractional crystallization: some mineralogic and petrographic constraints. J. Petrol., 27(5): 1095-1117.

**Zhao, T. and X. Deng (2016)**. Petrogenesis and Tectonic Significance of the Late Paleoproterozoic to Early Mesoproterozoic (~1.80–1.53 Ga) A-Type Granites in the Southern Margin of the North China Craton. In M. Zhai, Y. Zhao, & T. Zhao (Eds.), Main Tectonic Events and Metallogeny of the North China Craton Pp: 423-43. Singapore: Springer Singapore.

**Zhu, J. ; B. Rao ; X. Xiong ; F. Li and P. Zhang (2002):** Comparison and genetic interpretation of Li-F rich, rare-metal bearing granitic rocks. Geochimica, 31(2): 141-152.

## أصل النشأة وتمعدن جرانيت ابودباب الالبيتي: رؤى حول الجرانيت من النوع A الغني بالمعادن النادرة في الدرع العربي النوبي

**مصطفى محمد مجاهد[1]*، ماهر عبداللطيف العماوي[1]، عصران محمد عصران[2]، نسمة جمال محمود[1]**

[1]قسم الجيولوجيا، كلية العلوم، جامعة بنها، 13518 بنها، مصر

[2]قسم الجيولوجيا، كلية العلوم، جامعة سوهاج، 82524 سوهاج، مصر

تكوّن الدرع العربي انوبي في شمال شرق أفريقيا خلال التصادم النيوبروتيروزوي بين غندوانا الشرقية والغربية، وإغلاق محيط موزمبيق. بعد مرحلة ما بعد التصادم التي بدأت نحو 620 مليون سنة مضت، استقرّ الدرع بحلول نحو 540 مليون سنة مضت، وشهد تحركات صهرية ضافرت بتكوين جرانيتات غنية بالمعادن النادرة. يبرز جرانيت الألبايت بأبو الدبّاب في صحراء مصر الشرقية الوسطى بسبب محتواه العالي من النيبيوم، التانتالوم، القصدير، الزركونيوم والعناصر النادرة للأرض. ولا يزال نموذج تأصله موضع نقاش. تُظهر دراساتنا الميدانية والصخرية والمعدنيّة والجيوكيميائية المتكاملة أن هذا الجرانيت يتميز بمحتوى عالي نسبيا من الألمونيوم في حين ان محتواه من لسليما مرتفع جدًا، ويندرّج هذا الجرانيت تحت النوع الكلسي–قلويي بالغ التطور. كما أن هذا النوع من الجرانيت نشأ ضمن نظام تكتوني انتقالي في الدرع العربي النوبي. كما يُعرف بمعدل Rb/Sr مرتفع، ومحتوى غني بالـNb–Ta–Sn–Hf ، مع شذوذ سلبي واضح فيEu ، مما يتماشى مع مجموعة الجرانيت من النوع A الحاملة للموسكوفيت والمتطوّرة. وتشير دراساتنا الى ان مصدر هذا الجرانيت هو مصدر قشري قاري

حيث يرقّ الغلاف الصخري بفعل التمدد حراري أو حركة رافعة لحِمَم طبقة الوشاح مما يؤدي الى تراكم صهارة الوشاح والتي تمثل مصدر حراري يؤدي إلى ذوبان الميكا في الصخور القشرية. وهذه الصهارة الناتجة تكون غنية بالفلور وتسهّل تكوين جرانيّتات موسكوفيتية مثل أبو الدبّاب. كما أشرنا الى ان المصهور الناتج قد خضع لاثراءات غنية بالفلور الإلومينيوم ثم تعرضت لتبلور تجزيئي مطوّل ضمن ظروف صهارية–هيدرثرمالية، مولّدةً عدّة نُظم للتعدين على Ta–Nb–Sn وشبكات الغرايزن داخل الصدوع.